Reviews of Geophysics

REVIEW ARTICLE
10.1029/2024RG000857

Stemflow Hydrodynamics

Gabriel G. Katul[1], Bavand Keshavarz[2], Amirreza Meydani[3], and Delphis F. Levia[3,4,5]

[1]Department of Civil and Environmental Engineering, Duke University, Durham, NC, USA, [2]Department of Mechanical Engineering and Material Science, Duke University, Durham, NC, USA, [3]Department of Geography and Spatial Sciences, University of Delaware, Newark, DE, USA, [4]Department of Plant and Soil Sciences, University of Delaware, Newark, DE, USA, [5]Department of Civil, Construction, and Environmental Engineering, University of Delaware, Newark, DE, USA

Key Points:

- Stemflow hydrodynamic theories lag behind their counterparts for within-plant water delivery systems
- A juxtaposition of thin film approximation onto stemflow hydrodynamics is proposed
- Directions for future research topics suitable for doctoral dissertations are featured

Supporting Information:

Supporting Information may be found in the online version of this article.

Correspondence to:

G. G. Katul,
gaby@duke.edu

Citation:

Katul, G. G., Keshavarz, B., Meydani, A., & Levia, D. F. (2025). Stemflow hydrodynamics. *Reviews of Geophysics*, *63*, e2024RG000857. https://doi.org/10.1029/2024RG000857

Received 23 OCT 2024
Accepted 30 MAY 2025

Author Contributions:

Conceptualization: Gabriel G. Katul, Bavand Keshavarz, Amirreza Meydani, Delphis F. Levia
Formal analysis: Gabriel G. Katul, Bavand Keshavarz, Amirreza Meydani, Delphis F. Levia
Funding acquisition: Gabriel G. Katul
Investigation: Gabriel G. Katul, Bavand Keshavarz, Amirreza Meydani, Delphis F. Levia
Methodology: Gabriel G. Katul, Amirreza Meydani, Delphis F. Levia
Project administration: Gabriel G. Katul
Software: Gabriel G. Katul, Amirreza Meydani
Supervision: Gabriel G. Katul, Delphis F. Levia
Validation: Gabriel G. Katul
Writing – original draft: Gabriel G. Katul, Bavand Keshavarz, Amirreza Meydani, Delphis F. Levia

Abstract Stemflow hydrodynamics is the study of water movement along the exterior surface area of plants. Its primary goal is to describe water velocity and water depth along the stem surface area. Its significance in enriching the rhizosphere with water and nutrients is not in dispute. Yet, the hydrodynamics of stemflow have been entirely overlooked. This review seeks to fill this knowledge gap by drawing from thin film theories to seek outcomes at the tree scale. The depth-averaged conservation equations of water and solute mass are derived at a point. These equations are then supplemented with the conservation of momentum that is required to describe water velocities or relations between water velocities and water depth. Relevant forces pertinent to momentum conservation are covered and include body forces (gravitational effects), surface forces (wall friction), line forces (surface tension), and inertial effects. The inclusion of surface tension opens new vistas into the richness and complexity of stemflow hydrodynamics. Flow instabilities such as fingering, pinching of water columns into droplets, accumulation of water within fissures due to surface tension and their sudden release are prime examples that link observed spatial patterns of stemflow fronts and morphological characteristics of the bark. Aggregating these effects at the tree- and storm- scales are featured using published experiments. The review discusses outstanding challenges pertaining to stemflow hydrodynamics, the use of dynamic similarity and 3D printing to enable the interplay between field studies and controlled laboratory experiments.

Plain Language Summary Describing how water molecules move along the exterior of a plant surface remains a daunting challenge despite some 150 years of research and observations. While stemflow arriving onto the soil surface is usually a small percentage of incident rainfall (about 0.1%–10%), its significance is no longer in dispute and is gaining traction in multiple fields such as eco-hydrology, forest ecology, soil biogeochemistry and nutrient cycling, urban planning and green infrastructure, among others. This review seeks to mathematically describe the movement of water along the stem of individual plants using the conservation laws of mass and momentum when the water depth along the surface is sufficiently shallow compared to the overall path length the water traverses along the main stem—an approximation labeled as thin film. The review shows how stemflow hydrodynamics deserves its rightful place in the general area of fluid mechanics. Its coverage offers new generalizations and perspectives to thin film theories routinely used in engineering and material sciences. The topic also serves as fertile ground for graduate student dissertations concerned with developing fundamentals, welding vast knowledge from distinct disciplines together, and innovating experiments (laboratory and field) or numerical simulations in a manner that maintains high societal impact.

1. Introduction

Stemflow, the water that flows over the exterior of a plant's trunk or stem (e.g., see Figure 1) is receiving renewed interest in ecohydrology. While stemflow usually represents a small fraction (<12%) of gross incident rainfall for woody plants (J. Brown & Barker, 1970; Levia & Germer, 2015; Magliano et al., 2019; Martinez-Meza & Whitford, 1996) compared to throughfall or canopy interception, its role in directing and concentrating water, solutes (e.g., potassium, calcium, manganese), particulates, and metazoans (among others) from the canopy into the soil-root system can be substantial (Carlyle-Moses et al., 2018; Cayuela et al., 2019; Germer, 2013; Gersper & Holowaychuk, 1971; Levia & Frost, 2003; Llorens et al., 2022; Martinez-Meza & Whitford, 1996; Olson et al., 1981; Parker, 1983; Ptatscheck et al., 2018). Published dye experiments (Liang, 2020) have shown that stemflow allows solutes to enter the soil system through macro-channels that deliver nutrients to where they are most needed in the rhizosphere (M. Johnson & Lehmann, 2006; Martinez-Meza & Whitford, 1996; Schwärzel et al., 2012). Stemflow and soil moisture measurements already demonstrated that a significant portion of the water that falls onto the canopy is funneled and concentrated by the branches and stem, and is eventually routed to

Writing – review & editing: Bavand Keshavarz, Amirreza Meydani, Delphis F. Levia

the soil in a relatively narrow, asymmetrical band around the tree base (Imamura et al., 2017; Levia & Germer, 2015; Llorens et al., 2022; Pinos et al., 2021; Tischer et al., 2020; Voigt, 1960; Wu et al., 2024).

Of greater significance is the chemical composition of this water. The contact duration between water and the plant's exterior surface is longer for stemflow compared to throughfall. This extended contact enables efficient leaching and solute transport along trunk and stems (Parker, 1983). Quantitative reviews have shown that stemflow solute concentration usually exceeds throughfall concentration (Levia & Germer, 2015; Zhang et al., 2024). In some cases, stemflow can have a long-term imprint in the soil because of stemflow-induced soil acidification or the double funneling effect (Falkengren-Grerup & Björk, 1991; M. Johnson & Lehmann, 2006; Matschonat & Falkengren-Grerup, 2000). For this reason, stemflow is one of the main mechanisms responsible for the so-called soil biogeochemical hot-spots and hot-moments (Carlyle-Moses et al., 2018; Levia & Germer, 2015). The role of stemflow in aboveground water dynamics has and continues to receive research attention. Stemflow has been implicated in the diel patterns of aboveground water storage recharge that acts as buffer for reduced xylem water potential and maintains hydration of living tissue (Beckett et al., 2024). When the outer bark is wet enough, some tree species uptake stored water from the bark for internal use (Van Stan et al., 2021). These findings have been noted for some time now using spraying experiments. In these spraying experiments, water potential recovery in twigs occurred after bark water absorption commenced (Katz et al., 1989). For this reason, the movement of water from bark rays into the xylem has also been labeled in some studies as the "undervalued route of water transport" (Pfautsch et al., 2015; Van Bel, 1990). Similar conclusions have been drawn in relation to leaf hydration and surface water uptake of shoots (Fuenzalida et al., 2019). Water into the soil can increase through stemflow and throughfall during fog occurrences primarily from droplet formation onto the canopy surface (Olson et al., 1981; Roth-Nebelsick et al., 2012). A recent study demonstrated that woody surfaces of trees at and above about 2 m from the forest floor can uptake methane and result in a net tree methane sink (Gauci et al., 2024). The microbially mediated draw-down of methane on and in tree woody surfaces and tissues was found to be significant in tropical and temperate forests where stemflow plays a role in maintaining the health of such microbial communities. Research on acid rain interaction with plants also demonstrated that uptake and loss of ions through above-ground plant parts (cuticles and bark) can be substantial (Klemm et al., 1989). These exchanges remain understudied theoretically and experimentally partially due to stemflow hydrodynamics uncertainty.

While K. E. Ney was the first to measure stemflow (in 1870), it was W. Riegler (in 1881) who first linked canopy architecture to stemflow production (Riegler, 1881). Likewise, studies on water-bark interactions have a long tradition (about 150 years) in plant biology (Van Stan et al., 2021) as first reported by G. Kraus (in 1877). These studies began before Dixon and Joly (Dixon & Joly, 1894) put forth the cohesion-tension theory for water movement in the xylem (in 1894) and E. Münch proposed (in 1930) the osmoregulation hypothesis for water and sugar transport in the phloem (Munch, 1930). Despite earlier measurement leads in stemflow, a formulation for stemflow hydrodynamics that resembles in its predictive power the cohesion-tension theory for water flow in the xylem or the osmoregulation theory for water/sugar transport in the phloem (Jensen et al., 2016; Konrad et al., 2019) remains lagging or lacking altogether. This may appear surprising as stemflow is, to say the least, more visible to the naked eye than phloem or xylem water delivery systems in Figure 1. As shall be seen from this review, the mathematical formulation of stemflow hydrodynamics is far richer than those associated with either the xylem or the phloem, which may partly explain why a comparable theory to cohesion-tension or osmoregulation did not materialize. In continuum mechanics, the conservation of fluid mass and linear momentum, also known as the Navier-Stokes equation, when combined with the solute continuity equation provide a complete mathematical description of velocity, solute concentration and fluxes at a single point or a small representative elementary volume on the stem surface. Formulating the dominant forces within those equations and solving them along a complex branch-trunk geometry for transient rainfall remains a formidable challenge. Even by today's computational standards, the computational costs and the uncertain initial and boundary conditions required in such simulations remain prohibitive in virtually all eco-hydrological applications. For this reason, this review primarily focuses on stemflow hydrodynamics that seeks to describe the depth-averaged equations for water mass, momentum, and solutes. These equations link the depth-averaged water and solute fluxes and states to the local properties of the bark surface (e.g., roughness, wetness, leaching capacity), which makes them applicable in many geophysical and ecological applications. This starting point, focusing on water and solute fluxes, must be viewed as necessary but not sufficient for long-term ecosystem level biogeochemical cycling that requires, at minimum, upscaling the equations to tree scale following some approximation to the overall geometry (branch-

10.1029/2024RG000857

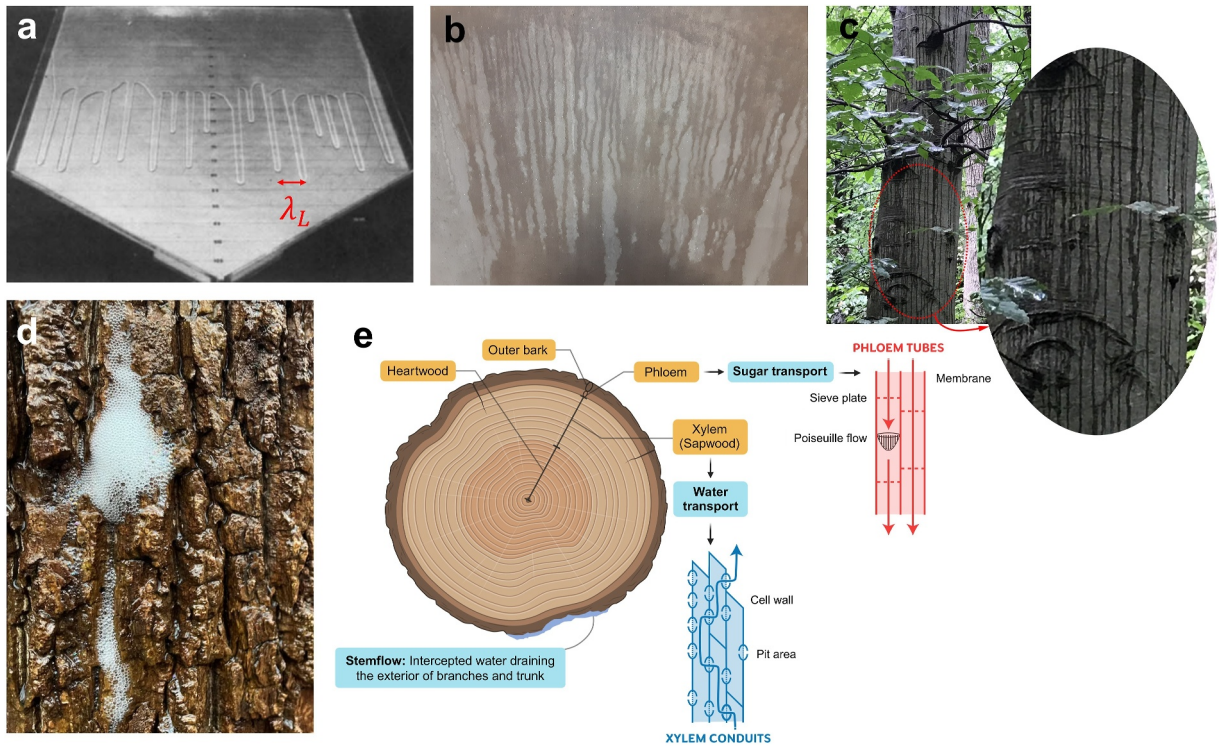

Figure 1. Panel (a) Lateral instabilities of a wetting front on an inclined slope. The photo is taken from Huppert (1982). The instabilities exhibit fingering with lateral wavelength (λ_L) that is independent of viscosity. Panel (b) Similar instabilities can be seen on a concrete vertical slab where the flow is from top to bottom (Photo credit: G. Katul). Panel (c) Fingering and preferential flow on a smooth-barked American beech tree (Photo credit: D. Levia). Panel (d) bubbling and high surfactant concentration (Photo credit: John Kelly, The Washington Post Picture of foamy bubbles form on the bark of a tree along Sligo Creek in Silver Spring (2024)). Panel (e) cross-section of a tree denoting various anatomical features, including subpanels of xylem conduits and phloem tubes from Jensen et al. (2016). Panel (e) was partly created in Biorender. Meydani, A. (2025) https://BioRender.com/c92x693. The xylem delivers water from the root to the leaf under tension whereas the phloem moves water and sugars from the leaf to other parts of the tree as needed for metabolic function.

stem configuration) of the tree (coarsest scale) and the micro-roughness properties of the bark (finest scale). Upscaling these equations to arrive at stemflow fluxes into the soil, even from the base of a single tree, requires coarse-graining non-linear and multi-scaled transport processes whose physical and chemical properties are rarely measured in field experiments. Nonetheless, those challenges will be flagged and theoretical, computational, and experimental tactics (laboratory and field) to be employed will be surveyed. Regarding the latter point, comparing laboratory and field studies requires a coverage of the principles of dynamic similarity (Bolster et al., 2011), which will be presented for the depth-averaged equations. This principle has a long history in physics and biology starting with the work of Galileo and Borelli in the 1600s (Galilei, 1914; Gunther, 1975), followed by Thompson (1915), Buckingham (1914), Rayleigh (1915), and many others reviewed elsewhere (G. West, 2018). Its usage remains under-utilized in the study of eco-hydrology in general and stemflow hydrodynamics in specific with some exceptions (Katul et al., 2019; Porporato, 2022).

2. Overview of Experimental Results

Studies of stemflow generation and its chemical composition have focused on three interrelated effects:

2.1. Biophysical Characteristics of Tree Species

Stemflow generation and its chemical composition are routinely linked to biophysical characteristics such as smooth versus rough bark, branching orientation, and the presence of epiphytes (André et al., 2008; Cape et al., 1991; Levia & Frost, 2003; Voigt & Zwolinski, 1964). Moreover, bacteria living on bark surfaces are usually more diverse than their leaf surface counterparts (Leff et al., 2015) so that stemflow leachates are altered to a greater extent than throughfall (Levia et al., 2011; Zhang et al., 2024).

2.2. Tree Size and Architecture

Stemflow generation is expected to scale with wetted trunk and branch surface areas, which are related to tree size by allometric relations (Whittaker & Woodwell, 1967). While empirical relations between measures of tree size (e.g., height, diameter, projected crown area, foliage amount) and stemflow generation have been reported for some 50 years now (J. Brown & Barker, 1970; Crockford & Richardson, 2000; Ford & Deans, 1978; Hanchi & Rapp, 1997; R. Johnson, 1990; Manfroi et al., 2004; Martinez-Meza & Whitford, 1996), these relations remain "diagnostic" rather than "prognostic" and sometimes controversial—meaning that stemflow from individual trees was variable but the variability was not explained by tree size such as trunk diameter or tree height (Loustau et al., 1992). One reason for this gap is that water collection is impacted by canopy structure (Aboal et al., 1999; Bialkowski & Buttle, 2015; Gonzalez-Ollauri et al., 2020; Iida et al., 2021; Levia & Germer, 2015), including factors such as branch number and branch inclination angle (Iida et al., 2021; Levia & Herwitz, 2002; Levia et al., 2015; Murakami, 2024) and whether trees are leafless or not (Iida et al., 2021). Experiments have reported some 80% of the impacting rainfall is channeled as branchflow when branch inclination angles exceed 60° above the horizontal (Herwitz, 1987). How intercepted water onto branches concentrates into rivulets (small streams) that flow beneath branches has been recently considered using laboratory experiments and hydrodynamic analysis (Puri et al., 2024). It was found that under certain conditions, rivulets do remain attached to branches by surface tension until they encounter the main tree trunk where they contribute to stemflow generation. When rivulets detach from parent branches, they concentrate throughfall into what is termed pour points (hotspots for throughfall). Laboratory experiments on cylindrical objects showed that rivulet formation rate does increase with increasing branch inclination angle to the horizontal axis and the formation rate did not vary appreciably with the water application rate. These laboratory studies support the earlier field studies on branchflow (Herwitz, 1987). Interestingly, the overall water collected at the end of the inclined cylindrical branches decreased with higher flow rates due flow instabilities. These instabilities are mainly due to rivulet thickness exceeding a certain threshold and contributing to throughfall instead of stemflow (Puri et al., 2024).

A recent synthesis, which is enriched with other data sources by us and presented here, has shown that the fraction of incident rainfall that generates stemflow is related to the ratio of the tree height H and crown width W defined in Figures 2a and 2b using

$$y_o = 10.47[1 - \exp(-0.38x_o)], \quad (1)$$

where y_o is the percentage of measured stemflow at the base of trees to incident rainfall (usually collected in an open clearing), and $x_o = (H/W) - 0.8$. While the determination of H is less ambiguous, the W in Figures 2a and 2b may also be inferred using multiple approaches. The first is using the projected crown area, which is the area used to convert stemflow from volume to equivalent depth in water balance studies. With this definition, some self-correlation is expected in the comparisons featured in Figure 2d. The second may define W as the horizontal width of the tree's crown measured as the maximum distance between the outer edges of the foliage. For large W (or low branch inclination angles from the horizontal), foliage interception and subsequent throughfall may out-compete stemflow generation by branches.

On long time scales (e.g., seasonal to annual) covering a large ensemble of rainfall events, an inverse relation between W and stemflow may be anticipated. However, larger H reflects larger surface area available for stemflow production and thus a positive relation between stemflow generation and H may be anticipated. For the combined data sources and a wide range in H/W values featured in Figure 2d, the empirical expression linking y_o to x_o explains some 70% of the variability in stemflow generation by rainfall with a coefficient of determination $R^2 > 0.7$. Another extensive study comparing stemflow production to rainfall for oaks and pines (burned and unburned) arrived at similar conclusions (Su et al., 2023) to what was found in Figure 2d for y_o. As noted earlier, such empirical expressions may emerge when stemflow to rainfall are determined over long time scales (seasonal to multi-year) and across a wide range of H/W values (a factor of 10).

The relation featured in Figure 2d tends to break-down when the focus is on a single storm event and/or when the range of H/W is too narrow. A case in point are the laboratory studies of stemflow on artificial trees made from wooden dowels (Dunkerley, 2014a). In those experiments, H/W did not vary as shown in Figure 2d. However, antecedent bark wetness, rainfall intensity variability (uniform vs. intermittent), and whether a drop-kinetic energy dissipation using a mesh was present or not did have appreciable impact on y_o for a near constant H/W. The

10.1029/2024RG000857

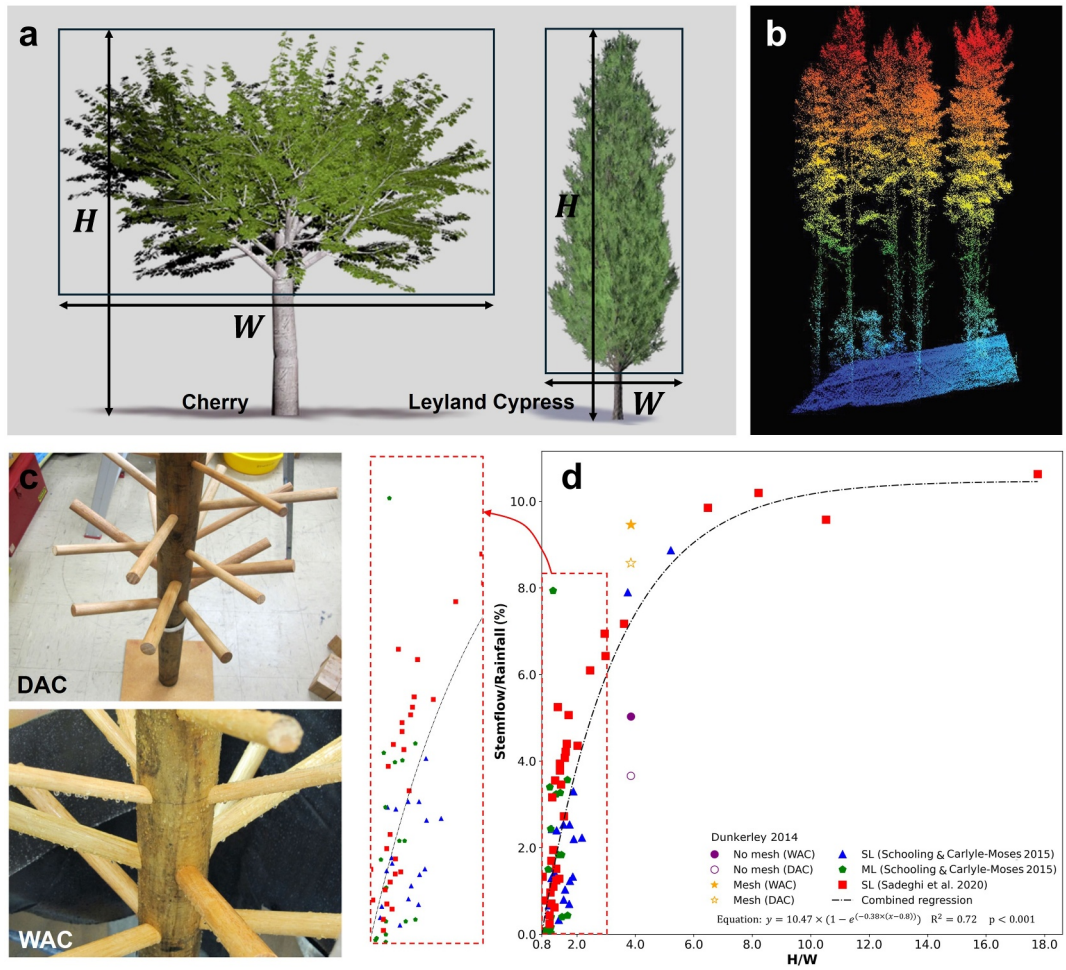

Figure 2. Panel (a) Sketch of H and W for wide (Cherry, 2024) and slender (Leyland cypress, 2024) tree geometries. Panel (b) These geometric features can be inferred from LiDAR remote sensing platforms (Roth et al., 2007). Panel (c) Laboratory measurements on wooden dowels collected for a constant H/W from Dunkerley (2014a). DAC and WAC denote dry and wet antecedent conditions. Panel (d) Relation between the long-term ratio of measured stemflow to incident precipitation or y_o in percent (ordinate) as a function of the height-to-width (abscissa) or H/W of trees assembled from a global database (Sadeghi et al., 2020) along with field experiments from isolated single-leader and multi-leader urban trees (Carlyle-Moses & Schooling, 2015; Schooling & Carlyle-Moses, 2015). SL and ML denote single-leader and multi-leader trees. The SL and ML urban data sets (Schooling & Carlyle-Moses, 2015) convert stemflow volume to equivalent water depth using projected crown area, which is common practice (Sadeghi et al., 2020). Some of the scatter may arise due to differences in the scaling variable used to convert stemflow volume to depth. Laboratory experiments are presented for DAC and WAC without and with a mesh placed above the wooden dowel to dampen the raindrop kinetic energy.

laboratory experiments do show that in the absence of a mesh (i.e., raindrops have high incident kinetic energy), the y_o (in percent) varied from 2.5 to 7.0 whereas in the presence of a mesh above the canopy, y_o varied from 7 to 11. Higher antecedent surface wetness (WAC) also resulted in higher y_o compared to drier antecedent conditions (DAC).

2.3. Hydroclimatic Variability and Antecedent Conditions

Stemflow volumes and leaching are influenced by clouds, rainfall depth class, rainfall intensity, angle of incident precipitation, air temperature, vapor pressure deficit, evaporation, and antecedent conditions, as reviewed elsewhere (Levia & Germer, 2015; Levia & Herwitz, 2000; Levia et al., 2010; Reid & Lewis, 2009; Schooling & Carlyle-Moses, 2015; Van Stan et al., 2014). The so-called funneling effect of branches is enhanced once branches are wet (Herwitz, 1987), suggesting that both intra-storm rainfall dynamics and vapor pressure deficit can play a role (Cayuela et al., 2018; Dunkerley, 2014a; Levia, 2003). These field studies are consistent with the

aforementioned laboratory experiments in Figure 2 where the stemflow to rainfall contrast for wet and dry wooden dowels is significant. All these effects encompass processes across a range of scales: (a) "local-scale," describing local surface properties and their interaction with moving water in Figure 1—including the generation of unstable fronts in smooth bark, (b) "tree-scale," referring to the multiple path lengths experienced from source to ground, (c) "forcing," the storm characteristics and other hydroclimatic descriptors (e.g., wind, temperature, vapor pressure deficit), and (d) "initial conditions," referring to antecedent conditions of the bark prior to stemflow generation. At the smallest scale, where the local bark properties are most relevant to water-solute interactions, the depth-averaged equations are subject to boundary conditions. In smooth bark as shown in Figure 1, the flow dynamics share resemblance to thin-films (Haas et al., 2011; Scholle & Aksel, 2001, 2003). Fingering patterns and other instabilities can arise (Huppert, 1982; Nittmann et al., 1985) speeding up the flow—especially at the fingertip. For rough bark, water and solutes are transported either through a network of interconnected ridges and furrows within the bark or along the bark surface that can be hydrodynamically rough, smooth, or transitional. Water flow responds to a number of forces including gravitational body forces, frictional surface forces (viscous laminar or turbulent stresses), and capillary line forces at the air-water interface. At the local scale, the movement of water resembles either a free surface flow or an anisotropic porous medium depending on the rainfall intensity and duration as well as evaporation and bark absorption. The geometric properties of each furrow (e.g., their length, angle, effective width, micro-roughness, and chemical properties) also vary along the branch and bark. Moving beyond the single furrow scale, connections between multiple furrows within the bark and ridges impose extra constraints that alter the overall stemflow in ways that remain to be explored. Due to the concentrated nature of stemflow inputs, the focus is woody surface flows (branches and trunks) rather than release throughfall that reaches the ground from either foliar or woody surfaces. As noted earlier, a plausibility argument for this focus is the longer residence times of intercepted water on woody surfaces than foliar surfaces (Nanko et al., 2022) that enrich chemical concentrations (Tucker et al., 2020).

Accommodating all aspects and path details of stemflow dynamics along with solute transport is well beyond the scope of a single study. The emphasis here is on processes and mechanisms likely to be common to all stemflow representation. More specifically, the focus is on the hydrodynamics of stems that differ in bark morphology. Addressing this component provides the groundwork necessary for a complete description of stemflow and solute transport. The time is ripe to confront these challenges given the rapid progress in measurements including optical measurements of surface cover such as LiDAR (Iida et al., 2021; R. Turner et al., 2014) or microwave remote sensing (Landy et al., 2014), high resolution imaging for surface features and rapid dye movement, computing and computational methods, multi-scale physics, and in theories dealing with transport and chemical transformation in physical and biological networks (Banavar et al., 1999; Câmara & Neto, 2009; García-Ros et al., 2019; Heaton et al., 2012; Ni & Leonard, 2005).

3. Theory

Because stemflow is very shallow (i.e. water depth is much smaller than transport distances that scale with H), the conservation equations used to describe its hydrodynamics throughout are based on their depth-averaged form unless stated otherwise. The two key governing equations are for water mass and solute mass along the stem. The depth-averaged mass conservation equations reveal the need to accommodate water sinks (sorption into the bark volume) and solute sources (leaching). An existing theory for the water sinks into the bark surface based on a porous media approximation is introduced and modifications due to hygroscopicity are featured. Likewise, the effective leaching of solutes is represented using formulations of maximum simplicity so as to enable the inclusion of findings from laboratory and field experiments into models of stemflow hydrodynamics. Both conservation equations (water and solutes) also require models for the depth-averaged flow velocity needed to describe water and solute fluxes. To describe the water velocity, the conservation of momentum is then considered at the surface of the bark. The momentum conservation requires a description of all the forces (gravitational, pressure, surface friction along the bark surface, and surface tension at the air-water interface) and the resulting acceleration from their imbalance (local and convective).

Accommodating all these forces and the acceleration operationally turns out to be a formidable challenge that has not been fully attempted for stemflow. To progress on some aspects of this issue, a number of simplifications and analogies to other well-studied flows are first reviewed. In particular, flow of water on a smooth bark shares a number of similarities to water flowing along a wet plate (rough or smooth) of finite width standing vertically. Thus, the conservation of water and solute mass as well as momentum commences with a brief review of the bulk

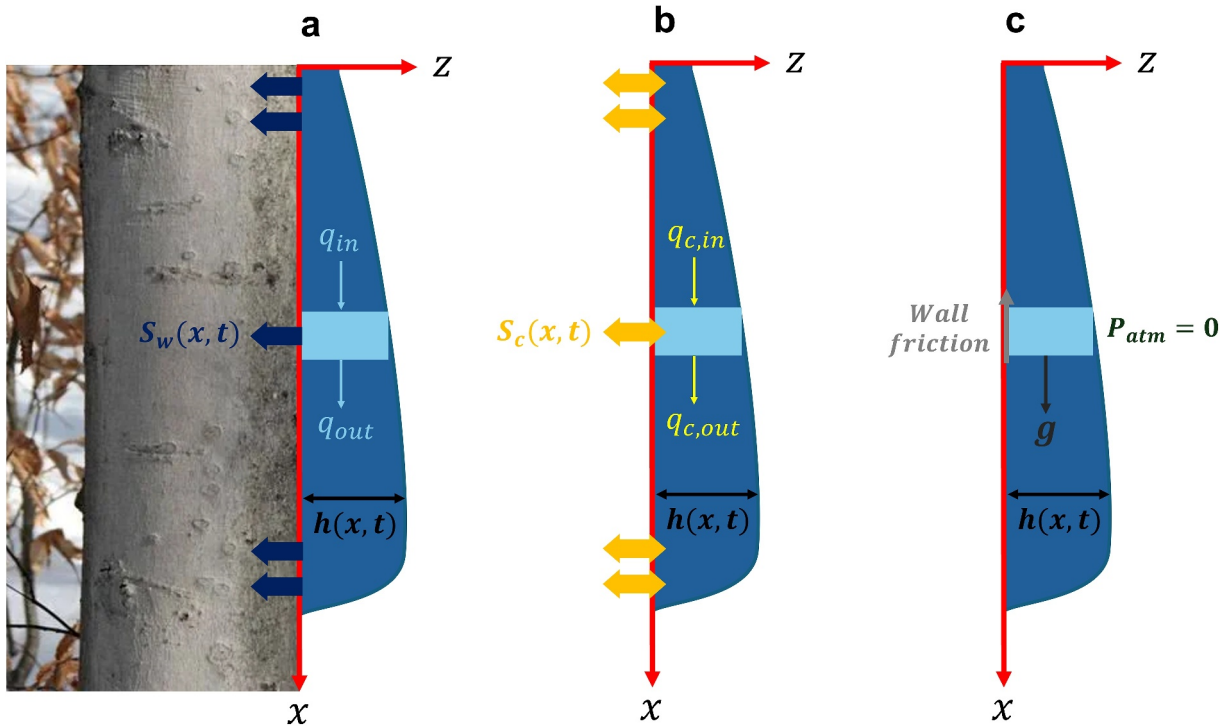

Figure 3. Definition sketch for the conservation of water mass (panel a), solute mass (panel b), and force balance (panel c). The x-axis is oriented along the direction of flow. The z-axis is orthogonal to the bark surface. The $h(x, t)$ is the water depth at position x and time t, q is the flux of water, S_w is the water uptake by the bark, q_c is the solute flux, and S_c is the solute leaching from the bark. The force balance includes pressure and gravitational forces, wall friction, and any curvature of the water surface determined from $\partial^2 h/\partial x^2$ as related to the balance between surface tension T and water pressure at the free surface (the latter are ignored for a vertical slope). The atmospheric pressure P_{atm} is assumed small compared to the water pressure at the curved interface.

velocity and water depth when the force balance for a given fluid element is restricted to the interplay between gravitational acceleration and viscous forces. Next, the addition of surface tension at the advancing front position is considered, which activates a number of mechanisms and instabilities that could not occur in a gravity-viscous stress balance scenario. Some aspects of roughness and higher Reynolds number effects are covered as well. The theory concludes with a proposition of a number of models to upscale these conservation equations to the entire tree system. The simplest are models based on nonlinear reservoirs whereby the canopy architecture is accommodated but not explicitly considered. While all the symbols are defined upon first occurrence in the text, a glossary is provided at the end of this review in "Glossary" section to facilitate readability.

3.1. Conservation of Water Mass

Figure 3 shows the control volume for the conservation of mass of a thin water film along a smooth bark surface (panel a) at position x characterized by a radially uniform water depth h along the local stem diameter D_s, a thickness dL along the vertical flow direction x. Assuming the density of water ρ is constant and $h/D_s \ll 1$ the changes in mass within an elementary volume $(\pi D_s)(dL)$ (h) in one-dimensional space along x yields

$$\frac{\partial \rho(\pi D_s\ dL)\,h}{\partial t} + \frac{\partial \rho(\pi D_s\ dL)\,q}{\partial x} = -\rho(\pi D_s\ dL)\,S_w, \tag{2}$$

where $h(x, t)$ is the depth of water at position x and time t, $q = u_{avg}h$ is the water flux, u_{avg} is the depth-averaged velocity at x and t, and as before D_s is the diameter of the stem at position x, dL is an incremental distance along direction x, and S_w is the loss of water into the bark. We choose to write these conservation laws in one spatial dimension using velocity and depth for simplicity. To be clear, a one-dimensional description is incomplete as spatial patterns such as fingering are inherently two-dimensional and cannot be reconciled with a one-dimensional approximation. However, such one-dimensional approximation suffices to illustrate the dominant terms in the mass balance responsible for water movement. For the purposes of further exploring these dominant mechanisms

involved in water movement, it is instructive to assume D_s uniformity in x though the conservation laws can readily accommodate such changes in D_s with x if known. Thus, for constant ρ and a D_s independent of x, the conservation of water mass reduces to its familiar form

$$\frac{\partial h}{\partial t} + \frac{\partial q}{\partial x} = -S_w. \tag{3}$$

The stemflow in volume per unit time at the base of the plant can be expressed as $Q = u_{avg}h(\pi D_s)$, where $u_{avg}h$ must be determined near the base of the tree. The conservation of water mass (in 1-D or 2-D) is one equation in 3 unknowns: h, q or $u_{avg} = q/h$, and S_w. Mathematical closure necessitates two additional equations. The first is a description of S_w and the second is the conservation of momentum to relate u_{avg} and h.

For S_w, it is assumed that the bark is a porous medium characterized by pore diameters much smaller than D_s. This porous medium is then described by a hydraulic conductivity $K(\theta)$, a porosity η_p, and a specific water capacity $c(\theta)$ (or equivalently, a pressure-volume relation), where the volumetric water content of the bark $\theta = V_w/V_b$ is the ratio of the stored volume of water within the bark V_w normalized by the total bark volume V_b. The degree of bark saturation, which varies between 0 and 1, can also be approximated by θ/η_p. This degree of saturation choice may be more convenient to use. When $\theta = \eta_p$, the bark is fully saturated and when $\theta < \eta_p$, the bark is deemed unsaturated. When the flow of water from the exterior film into the bark volume is laminar, then Darcy's law applies and

$$S_w = -K(\theta)\frac{\partial \psi}{\partial z} = -K(\theta)\frac{\partial \psi}{\partial \theta}\frac{\partial \theta}{\partial z} = -D(\theta)\frac{\partial \theta}{\partial z}, \tag{4}$$

where S_w must be interpreted as volume of water entering the bark per unit area orthogonal to the flow direction (curved here because of D_s) per unit time, $D(\theta) = K(\theta)/c(\theta)$ is known as the liquid water diffusivity formed from the unsaturated hydraulic conductivity and the pressure-volume relation where $c(\theta) = (\partial\psi/\partial\theta)^{-1}$ is the specific water capacity of the bark, and $\psi(\theta)$ is the unsaturated water potential within the bark measuring the energy needed to extract water being held by capillary forces inside the bark medium. Stated differently, ψ is the tension that must be applied to extract water from within the bark at a given bark wetness θ. With this background, the conservation of water mass within the bark volume is given by its own continuity

$$\frac{\partial \theta}{\partial t} = \frac{\partial}{\partial z}D(\theta)\frac{\partial \theta}{\partial z}. \tag{5}$$

Equation 5 may be solved under a set of restrictive assumptions for the water flux entering the bark when the bark has an initial and uniform (in z) moisture content $\theta_i < \theta_o$, where θ_o is the moisture of the bark surface after the advancing front arrives at this location (i.e. $h > 0$). When the effects of the surface water continuity are transmitted into the bark using a constant θ_o, the water loss from the surface into the bark is given by Philip (1957)

$$S_w = \frac{1}{2}S_p t^{-1/2}, \tag{6}$$

where S_p is known as the sorptivity of water onto the bark surface. The S_p can be related to $D(\theta)$ using (Parlange, 1975)

$$S_p^2 = 2\sqrt{\theta_o - \theta_i}\int_{\theta_i}^{\theta_o}\sqrt{\theta - \theta_i}D(\theta)d\theta, \tag{7}$$

where θ_i is the initial bark water content before the arrival of the wetting front, and θ_o as before is the water content at the surface after the arrival of the wetting front. Some studies have experimentally explored the hygroscopic properties of bark (i.e., the ability of bark to uptake water vapor from the atmosphere during dry periods) that are likely to set θ_i. These studies demonstrated that the ability of bark to absorb water vapor during non-rainfall periods leads to a partial saturation of bark tissues during such dry periods that then alter the rate of bark saturation during rainfall (i.e., reducing $\theta_o - \theta_i$ and increasing θ_i). The θ_i is a function of the internal bark structure including η_p and bark density that varies among species (Ilek et al., 2021). If the bark is initially dry (i.e., $\theta_i \ll \eta_p$

and the arrival of the front saturates the bark surface, then θ_i can be ignored relative to θ_o and $\theta_o = \eta_p$). An intrinsic sorptivity given by $S_I = (\nu\rho/\sigma)S_p$ can also defined and this S_I, as with intrinsic permeability, is only dependent on the bark medium—not the fluid. Here, ν is the kinematic viscosity and σ is the surface tension parameter for water. It is evident that any description of stemflow requires a concentrated effort on measuring bark hydraulic properties for different bark types and wetness conditions.

3.2. Conservation of Solute Mass

As before, a unidirectional flow in Figure 3 is assumed along x. The solute mass under consideration at x and t is defined using solute concentration $C(x, t)$ in mass of solutes per mass of water and the incremental water volume $(\pi D_s)(h)(dL)$. Thus, the conservation of solute mass leads to

$$\frac{\partial}{\partial t}(\pi D_s h\ dL\rho C) + \frac{\partial}{\partial x}\left(\pi D_s h\ dL q_c\right) = (\pi D_s h\ dL)\rho S_c, \tag{8}$$

where q_c is the solute flux and S_c is the solute net exchange between the bark surface and the flow (leaching in most instances). Once again, for a D_s independent of x and a constant ρ, this balance reduces to

$$\frac{\partial(h\ C)}{\partial t} + \frac{1}{\rho}\frac{\partial\left(h\ q_c\right)}{\partial x} = (h)S_c, \tag{9}$$

which is entirely kinematic. As before, conservation of solute mass provides one equation in three unknowns: S_c, q_c, and C. As with the conservation mass of water, two additional equations must be supplied to mathematically close the solute mass transport problem. The solute flux q_c can be expressed by its conventional form—an advective and dispersive transport given by

$$q_c = \rho\left(u_{avg}C - D_T\frac{\partial C}{\partial x}\right), \tag{10}$$

where D_T is the total diffusion coefficient that includes both molecular (D_m) and dispersive (D_d) contributions (i.e., $D_T = D_m + D_d$). The dispersive term arises due to area-averaging of an inhomogeneous velocity field within h. For laminar flow conditions, the dispersive contributions to q_c are dominated by the well-studied Taylor dispersion given by Heaton et al. (2012), Taylor (1953)

$$\frac{D_d}{D_m} = g_f Pe^2, \tag{11}$$

where $Pe = u_{avg}l_o/D_m$ is a Peclet number measuring the advective to diffusive transport, l_o is a characteristic length scale (radial or vertical), and g_f is a factor that depends on the cross-sectional geometry. The original Taylor dispersion in closed tubes yields $l_o = r$ (r is the pipe radius) and $g_f = 1/48$. In open channels (more appropriate to stemflow), $g_f = 2/105$ and $l_o = h$ for wide rectangular channels (Chikwendu, 1986)—meaning the furrow width is much larger than h. For a turbulent flow, the dispersion coefficient $D_d = \alpha_d h u_*$ (Fischer, 1973; Taylor, 1954), where α_d depends on the geometry ($\alpha_d \approx 10$ for wide open channels) and u_* is the friction velocity (to be discussed later on in the context of momentum conservation).

With regards to the function S_c, a model of maximum simplicity that includes only leaching may be employed and is given as

$$S_c = \frac{C_{sat} - C}{\tau_c} = k_c\left(1 - \frac{C}{C_{sat}}\right), \tag{12}$$

where $k_c = C_{sat}/\tau_c$, τ_c is a characteristic time it takes to saturate water with solutes (e.g.., potassium, calcium, magnesium) starting from $C = 0$ or some other reference concentration, and C_{sat} is the solute concentration near the saturation limit of water. This representation introduces a new time scale, τ_c. It is customary to compare this time scale to the solute transport time scale by advection, given as L/u_{avg}, where L is the transport distance

—which is commensurate with H. The significance of the leaching mechanism may be compared to the advective transport using the so-called Damköhler number (Da), a dimensionless number that compares the leaching time scale to the advective time scale and is given by

$$Da = \frac{\tau_c u_{avg}}{L}. \tag{13}$$

A large Da implies that leaching is slow compared to advection and can be ignored. Conversely, a small Da means that advection may be ignored relative to leaching, and leaching dominates the temporal dynamics of C. It is instructive to ask what should be u_{avg} for leaching to be commensurate with advection. Setting $Da = 1$ yields a $u_{avg} = L/\tau_c$. For the solutes of interest in stemflow, including potassium, calcium, or magnesium, τ_c is on the order of 10–100 hr (Tucker et al., 2020). For a $L = 10$ m tall tree, a $Da = 1$ yields $u_{avg} = 0.1$–1 m/hr. Typical stemflow velocities are on the order of 10 m/hr (Tucker et al., 2020). This finding implies that C will remain sufficiently small compared to C_{sat} and advection is a significant contributor to solute transport along the stem. Equation 12 may also be generalized as

$$S_c = k_c\left(1 - \frac{C}{C_{sat}}\right)^n. \tag{14}$$

For $n = 0$, leaching is a constant input from the bark into the thin water film. For $n = 1$, leaching is a first-order generation process as before. Typical values for C_{sat} for potassium, calcium, and magnesium are 6.0, 26, and 6 mg/l, respectively (Tucker et al., 2020). Laboratory values of k_c in the literature are adjusted to account for the leaching surface area per volume of water. These values are 0.17 mg/cm^2/hr for potassium, 0.03 mg/cm^2/hr for calcium, and 0.04 mg/cm^2/hr for magnesium. For $n > 1$, the S_c resembles higher-order generation mechanisms as may be encountered in heterogeneous chemical systems due to the presence of chemical segregation or blockage of some distant molecules to accessing the depositing surface (i.e., bark). Such models can also arise when τ_c is no longer constant and becomes dependent on C, especially at high C.

To date, the most applicable model for the leaching of base cations and other substances of interest (e.g., boron, manganese, dissolved organic carbon) in stemflow is a binding/unbinding process with $n = 1$ (Segel & Edelstein-Keshet, 2013). To solve this equation for $C(x, t)$, the u_{avg} must be solved first. Moreover, k_c, C_{sat}, and n as well as a description of D_d are needed, the latter also requiring u_{avg}. The u_{avg} may be interpreted as momentum per unit mass (or concentration of momentum on a mass basis), which is why the conservation of momentum is now considered.

3.3. Conservation of Momentum: A Simplified Analysis

As a starting point, a simplified analysis that begins by assuming a balance between the frictional surface force and the gravitational body force is considered. The goal of this illustration is to highlight the role of several bark (e.g., rough vs. smooth) and flow (laminar vs. turbulent flows) properties prior to presenting an enriched version of the conservation of momentum that accommodates line forces and non-steadiness.

The gravitational force F_g acting on a fluid volume of small length dL along flow direction x and cross-sectional area $\pi D_s h$ is,

$$F_g = \rho(\pi D_s h dL)\, g \tag{15}$$

where g is the gravitational acceleration. This gravitational force is balanced by wall friction that is characterized by a wall stress τ_W acting uniformly on the planar area $\pi D_s dL$. Equating the driving force to the resistance force in the vertical direction (i.e. x) yields

$$\frac{\tau_W}{\rho} = u_*^2 = gh, \tag{16}$$

where u_* is known as the friction velocity and may be viewed as a kinematic description of the wall stress. Furthermore, representing the wall stress using a quadratic drag law with a drag coefficient C_d and average velocity u_{avg} results in

$$\frac{\tau_W}{\rho} = C_d u_{avg}^2. \tag{17}$$

It is customary to use the so-called Darcy-Weisbach friction factor f instead of C_d, where $C_d = f/8$. Thus, a balance between gravitational forces and frictional forces (i.e., no acceleration) results in an independent relation between h and u_{avg} given by

$$u_{avg} = \left(\frac{8}{f}\right)^{1/2} (gh)^{1/2}. \tag{18}$$

The simplified force balance in the vertical for steady and uniform flow enabled an independent link between u_{avg} and h. This link can be used to mathematically close the conservation of water and solute masses provided S_w and S_c are specified or modeled. The challenge now is to describe C_d or f for the bark surface, which is no trivial task. Drawing on what is known about f from pipe flow and open channel flow, two "end-member" cases are considered: The first is a laminar flow case over a smooth bark, and the second case is turbulent flow over a very rough bark, where the bark is characterized by a mean mirco-roughness height r. From the Moody diagram (Moody, 1944), f varies with the relative roughness r/h and the so-called Reynolds number $\mathrm{Re} = u_{avg}h/\nu$—but only one of these two quantities is pertinent at the two end-member limits. For the laminar flow case where $\mathrm{Re} < 100$, inserting $f = 24/\mathrm{Re}$ as derived from the Moody diagram and re-arranging yields,

$$u_{avg} = \frac{1}{3}\frac{g}{\nu}h^2. \tag{19}$$

The $f = 24/\mathrm{Re}$ can also derived from the depth-integrated Navier-Stokes equations for laminar flow as discussed elsewhere (Jeffreys, 1930). The flow rate per unit width $q = u_{avg}h$, which is more convenient to link to rainfall or stemflow production. In the laminar flow regime, this flow rate can be used to define a so-called Nusselt thickness (D'Alessio et al., 2009) given by

$$h_N = \left(\frac{3\nu q}{g}\right)^{1/3}. \tag{20}$$

For the turbulent flow case where $\mathrm{Re} >> 1{,}000$ and $r/h << 1$, the Moody diagram for open channels estimates $f = 0.26(r/h)^{1/3}$ (Katul et al., 2002), and

$$u_{avg} = \left(\frac{8g}{0.26r^{1/3}}\right)^{1/2} h^{2/3}. \tag{21}$$

The scaling between f and r/h is known as the Strickler scaling and, when imposed, reduces this equation to Manning's formula (Bonetti et al., 2017). In this case, Manning's formula for a vertical slope with $u_{avg} = (1/n_M)h^{2/3}$ is recovered provided Manning's roughness n_M is given by

$$n_M = \left(\frac{0.26}{8g}\right)^{1/2} r^{1/6} = 0.06r^{1/6}. \tag{22}$$

A recent study estimated Manning's roughness for burned ($n_M = 0.05$) and un-burned ($n_M = 0.08$) pine bark (Zhang et al., 2023) assuming turbulent flow. Based on Equation 22, the corresponding mean roughness values are $r = (n_M/0.06)^6 = 0.34$ m (burned) and $r = 5.5$ m (un-burned). In both cases, the reported mean protrusion depth of the bark surface is on the order of 4 mm. This means that the $r/h \ll 1$ is unlikely to be satisfied and n_M cannot be independent of h (Katul et al., 2002) or the measured flow is unlikely to be turbulent.

The main message from the simplified analysis here is that the stemflow velocity can be expressed as $u_{avg} = ah^b$, where a and b depend on the flow type (laminar or turbulent) and bark roughness (smooth or fully rough). Under some idealized conditions, a and b can be theoretically predicted when using the so-called Moody diagram (Moody, 1944) assuming stemflow resembles an open channel on a steep slope. A $u_{avg} = ah^b$ may be a more

general feature of the simplified momentum balance though the coefficients a and b may not be readily derived from a Moody type chart and require their own analysis. Toward this end, it is convenient to re-write Equation 18 as

$$Fr = \frac{u_{avg}}{\sqrt{gh}} = \left(\frac{8}{f}\right)^{1/2}, \tag{23}$$

which shows that "resistance" laws describing u_{avg} and h along the bark can be expressed in terms of a relation between the so-called Froude number (Fr) measuring inertia to the (external) gravitational force, and f, a dimensionless drag coefficient that varies with the Re (measuring inertia to viscous forces) and relative roughness r/h (i.e., connected to bark properties). A dynamically interesting outcome here is that u_{avg} appears to be related to h instead of $\partial h/\partial x$ as might be anticipated from a Darcy law (G. Brown, 2002; Darcy, 1856) or a Hagen-Poiseuille's equation (Sutera & Skalak, 1993). One other dimensionless number that routinely emerges in thin-film applications is the Galilei number (Ga), also referred to as the Galileo number. The Ga is used to assess the relative importance of gravitational forces to viscous forces and is given by

$$Ga = \frac{h^3 g}{\nu^2} = \left(\frac{Re}{Fr}\right)^2. \tag{24}$$

It is listed here for completeness as it is related to two other dimensionless quantities already being considered: Re and Fr.

3.4. Conservation of Momentum: An Expanded Analysis

The imbalance between all the forces acting on a fluid volume and the resulting acceleration along a vertically inclined plane must be considered in the expanded analysis at a point on the bark surface. This analysis leads to the following outcome:

$$\underbrace{\frac{\partial u_{avg}}{\partial t}}_{\text{Local Accel.}} + \underbrace{u_{avg}\frac{\partial u_{avg}}{\partial x}}_{\text{Advective Accel.}} + g\left(\underbrace{\frac{f}{8}\frac{u_{avg}^2}{gh}}_{\text{Friction}} - \underbrace{1}_{\text{Weight}} - \underbrace{l_{\text{cap}}^2\frac{\partial^3 h}{\partial x^3}}_{\text{Surf. Ten.}}\right) = 0. \tag{25}$$

The first term arises due to unsteadiness in the flow, the second arises due to inertia, the third term is the wall friction earlier discussed, the fourth term is the gravitational force, and the last term arises due to surface tension, where $l_{\text{cap}} \equiv \sqrt{\sigma/\rho g}$ is the capillary length that depends on the interfacial tension of water and air σ. Equation 25 resembles the standard shallow water (or Saint Venant) equation (de Saint-Venant, 1871) with two important exceptions. The first is that the mean pressure gradient is canceled (small angle approximation no longer applies to stemflow) and the second is the addition of surface tension effects.

The genesis of the surface tension term in the present form commences by assuming a mechanical equilibrium at the free air-water interface of the advancing front. This equilibrium requires that the imbalance between the exterior pressure (atmospheric) and interior pressure (water pressure at the air-water interface P_s) be carried by surface tension normal to the air-water interface. This equilibrium leads to the Young-Laplace equation given as Anderson et al. (2006)

$$P_s - P_{atm} = \frac{\sigma}{R_s}, \tag{26}$$

where P_{atm} is the atmospheric pressure (=0), P_s is the water pressure component at the curved air-water interface, and $1/R_s = -\nabla.\mathbf{n}$ is twice the mean curvature for the water surface that can be determined from the spatial variations of the unit normal vector $\mathbf{n}$. In the limit of 2D thin layers, the mean curvature can be approximated from $\partial^2 h/\partial x^2$. Once again, this curvature is likely to be large at the advancing front (or the tip of a finger instability) but perhaps less so elsewhere in the flow. The Young-Laplace equation estimates the air-water interfacial pressure

gradient $-\partial P_s/\partial x = \sigma\partial^3 h/\partial x^3$. The significance of surface tension in the conservation of momentum is often referenced to two other terms: the gravitational force and the inertial term. Thus, it is customary to introduce new dimensionless numbers for this comparative purpose—the Bond number (*Bo*), the Weber number (*We*), and the Kapitza number (*Ka*). They are given by

$$Bo = \frac{\rho g l^2}{\sigma} = \frac{l^2}{l_{\text{cap}}^2}; We = \frac{\rho u_{\text{avg}}^2 l}{\sigma}; Ka = \frac{\sigma}{\rho g^{1/3}\nu^{4/3}}, \tag{27}$$

where l is a characteristic length scale describing the longitudinal wavelength of the curvature of the water surface required for surface tension to act on (and differs from l_o) introduced in *Pe*, and $l_{\text{cap}} = \sqrt{\sigma/(\rho g)}$ is the capillary length whereby the gravitational forces and surface tension are in balance. For water, $\sigma = 0.078$ N m^{-1}, $g = 9.8$ m s^{-2}, and $\rho = 1{,}000$ kg m^{-3} resulting in $l_{\text{cap}} = 2.8$ mm. When $l/l_{\text{cap}} < 1$, surface tension effects may overcome gravitational forces and momentarily arrest stemflow. This may occur when the micro-roughness elements along the bark scale with l, the wavelength of the water surface profile. For these cases, the water may be held momentarily by surface tension within the bark fissures and furrows until sufficient amounts of accumulated water increases the gravitational force and overcome the surface tension forces. In such cases, stemflow resembles an intermittent accumulation-release mechanism or what may be labeled as a slip-stick phenomenon (Berman et al., 1996; Yan et al., 2023) in physics. The *Ka* is deemed as a material property that measures the relative importance of surface tension forces to inertial forces. For water flowing along a vertically inclined plane, $Ka = 3.4 \times 10^3$. The *Ka* plays a central role in the study of wave formation and instabilities leading to turbulence in thin films. At very large Re (≥1,000), waves observed on a falling film have wavelengths comparable to or shorter than h_N (Chang, 1994). Wavy patterns in stemflow are occasionally observed and thus, it is interesting to ask what is the magnitude of h_N for stemflow q reported (or estimated) in few field studies. For this illustration, a rainfall event of 25 mm in 18 hr that lead to an average 174 cm^3 per 5 min in stemflow and a peak of 980 cm^3 per 5 min is used (Tucker et al., 2020). The measured tree diameter D_s in this case study was 0.49 m. Thus, assuming stemflow is a uniform sheet along the entire circumference and the flow is laminar results in $h_N = 4.9 \times 10^{-3}$ mm. Using the peak flow rate instead increases h_N to $h_N = 8.7 \times 10^{-3}$ mm. These measurements were conducted for a rough bark with a furrow-ridge configuration. If the flow was assumed to be restricted to the furrow component only, the effective width drops by a factor of 87 and the $h_N = 3.2 \times 10^{-2}$ mm at the average flow rate and $h_N = 5.7 \times 10^{-2}$ mm at the peak flow rate. In all cases, this h_N remains some 2–3 orders of magnitude smaller than $l_{\text{cap}} = 2.8$ mm. However, l_{cap} is commensurate with the mean width of each furrows (=5.6 mm). These calculations are suggestive that surface tension can be of significance in such furrow-ridge bark roughness configurations when u_{avg} is small.

3.5. Dynamic Similarity: From Laboratory Experiments to Field Studies

Since its introduction in the early 1980s (Kodama, 1981), 3D printing will undoubtedly become popular in laboratory studies of stemflow hydrodynamics. The 3D printing builds physical objects from a digital computer aided design that involves layer-by-layer construction of physical objects such as synthetic trees. How can such technological advance enable efficient use of laboratory studies of stemflow necessitates linking the reduced geometry of the 3D printed object to the altered hydrodynamics and dominant force balance. In fluid mechanics, dimensionless numbers such as Re, *Fr*, *We* or *Bo* all have length scales (e.g., h, l_o, l, r, etc…). Preserving all these dimensionless numbers in laboratory studies enables links between laboratory dimensions and real-tree dimensions. Down-scaling geometry here requires reductions in H and W while preserving H/W to maintain long-term partition of rainfall to stemflow as discussed in Figure 2. This "shrinkage" of geometric features of trees (e.g. H and W) means that all the other absolute length scales (e.g. l, l_o, r, or L) relative to water properties (e.g. ν or σ) employed in the dimensionless numbers, summarized in Table 1, must also be reduced. This reduction alters the dominant force balance in the laboratory compared to field conditions. The "mapping" between the reduced geometric lengths required for laboratory studies while preserving the relative significance of the dominant forces governing the stemflow hydrodynamics in ecosystems requires matching all the dimensionless numbers simultaneously in Table 1. This matching may be partly achieved by employing fluids other than water or air to adjust the fluid properties such as density, viscosity, or surface tension in laboratory studies so as to preserve these dimensionless numbers. A weaker constraint is commonly used in practice that ensures laboratory studies match "flow regimes" expected in field studies such as laminar versus turbulence, reduce or enhance surface tension,

Table 1
Dimensionless Numbers and Formulas

Dimensionless number	Description
$Bo = \rho g l^2/\sigma$	Bond number
$Da = \tau_c u_{avg}/L$	Damköhler number
$Fr = u_{avg}/\sqrt{gh}$ ($=\sqrt{8/f}$ in the inertialess limit)	Froude number
$Ga = h^3 g/(\nu^2) = (Re/Fr)^2$	Galilei number
$Ka = \sigma/(\rho g^{1/3}\nu^{4/3})$	Kapitza number
$Pe = u_{avg} l_o/D_m$	Radial Peclet number
$\mathrm{Re} = u_{avg} h/\nu$	Reynolds number
$We \equiv \rho u_{\mathrm{avg}}^2 l/\sigma$	Weber Number

among others. The weaker matching ensures that the interplay between the dominant processes in laboratory studies and in field studies are commensurate (but not identical). However, the precise matching of all the dimensionless numbers can be by-passed provided the dominant regimes are captured by the experiments.

4. Applications to Published High Frequency Stemflow Experiments

A number of field experiments have published graphical representations of precipitation and stemflow at high frequency (e.g., 5 minutes or less) that have provided insights into stemflow patterns at the intrastorm scale (Levia et al., 2010; Reid & Lewis, 2009; B. Turner et al., 2019). In general, high temporal frequency stemflow experiments may be sensitive to the details of stemflow hydrodynamics compared to long term measurements such as those featured in Figure 2. A sample of those studies are digitized by us and used to explore simplified stemflow models.

Figure 4 presents normalized cumulative precipitation versus normalized cumulative stemflow for tropical trees and babassu palms across differing rainfall events in Brazil taken from Germer et al. (2010). Five published time series, shown in Figure 7 of the original source (Germer et al., 2010), were collected on a 5-min interval and digitized by us for the babassu palm. The precipitation time series were collected in a forest clearing. To underscore the conclusions in the original study (Germer et al., 2010), the digitized data are presented in Figure 4 and compared to their original Figure 8. The one-to-one line presented reflects expectations from a single proportional relation between accumulated precipitation (P) and accumulated stemflow (Q). For reference, another data set for *Fraxinus pennsylvanica* Marshall (green ash) tree (British Columbia) with $H = 7.8$ m and stem diameter $D_s = 0.108$ m is also presented in Figure 4 (black line labeled as reference storm) for comparison (B. Turner et al., 2019). The analysis confirms that on short time scales (i.e., 5 min), local stemflow is not proportional to local rainfall as evidenced by the departure from the one-to-one line. The digitized stemflow associated with the five storms in Figure 4 are also analyzed in phase space. The phase space is a plot representing measured stemflow $Q(t)$ at the base of the tree versus measured dQ/dt, whereby dQ/dt was estimated using forward differences $\Delta Q/\Delta t$ with $\Delta t = 5$ min. To allow for comparisons across tree species and storm types, the $Q(t)$ for each storm across all data sets are normalized by the total reported stemflow amount (i.e., $Q_{Total} = \sum Q$). The time in the computed dQ/dt is also normalized using the total duration of finite rainfall T_p (i.e., the effect of funneling ratio cancels in this representation). In the phase-space representation, a number of common features across storms and species become evident. For large $Q(t)/Q_{Total}$, the positive dQ/dt events (wetting phases) are larger in magnitude than their negative counterpart (recession phases). This behavior is the hallmark of hysteresis (i.e., loops in phase space) arising from the non-linearity in stemflow hydrodynamics responding to rainfall.

To explain these patterns in phase space, a model of maximum simplicity linking stochastic rainfall inputs to stemflow generation at the base of the tree is a 'lumped' model, often referred to as the non-linear reservoir model. This approach is inspired by field studies that show how bark surface area can operate as a water storage medium when linking precipitation to stemflow (André et al., 2008; Levia et al., 2010). The reference storm whereby stemflow was optically measured is used for illustration of such a model given the better resolution of ultrasonic measurements when compared to standard tipping bucket gauges. Ultrasonic measurements detect changes in transit times of sonic waves as water moves. They are often conducted by routing stemflow onto an open container and measuring changes in transit time of sonic waves faster than 5 min intervals or so. The branches are presumed to capture and route rainfall onto a main cylindrical stem rapidly as may be expected from rivulet formation (Puri et al., 2024) and short-distance branch transport. The main stem is assumed to have a diameter D_s and surface area $A_s = (\pi D_s)H$.

The lumped model conserves water mass but "lumps" the entire stemflow hydrodynamics along the bark into a single "storage-outflow" relation or velocity-head relation (i.e. u_{avg} related to h). The water mass conservation equation can now be expressed as

10.1029/2024RG000857

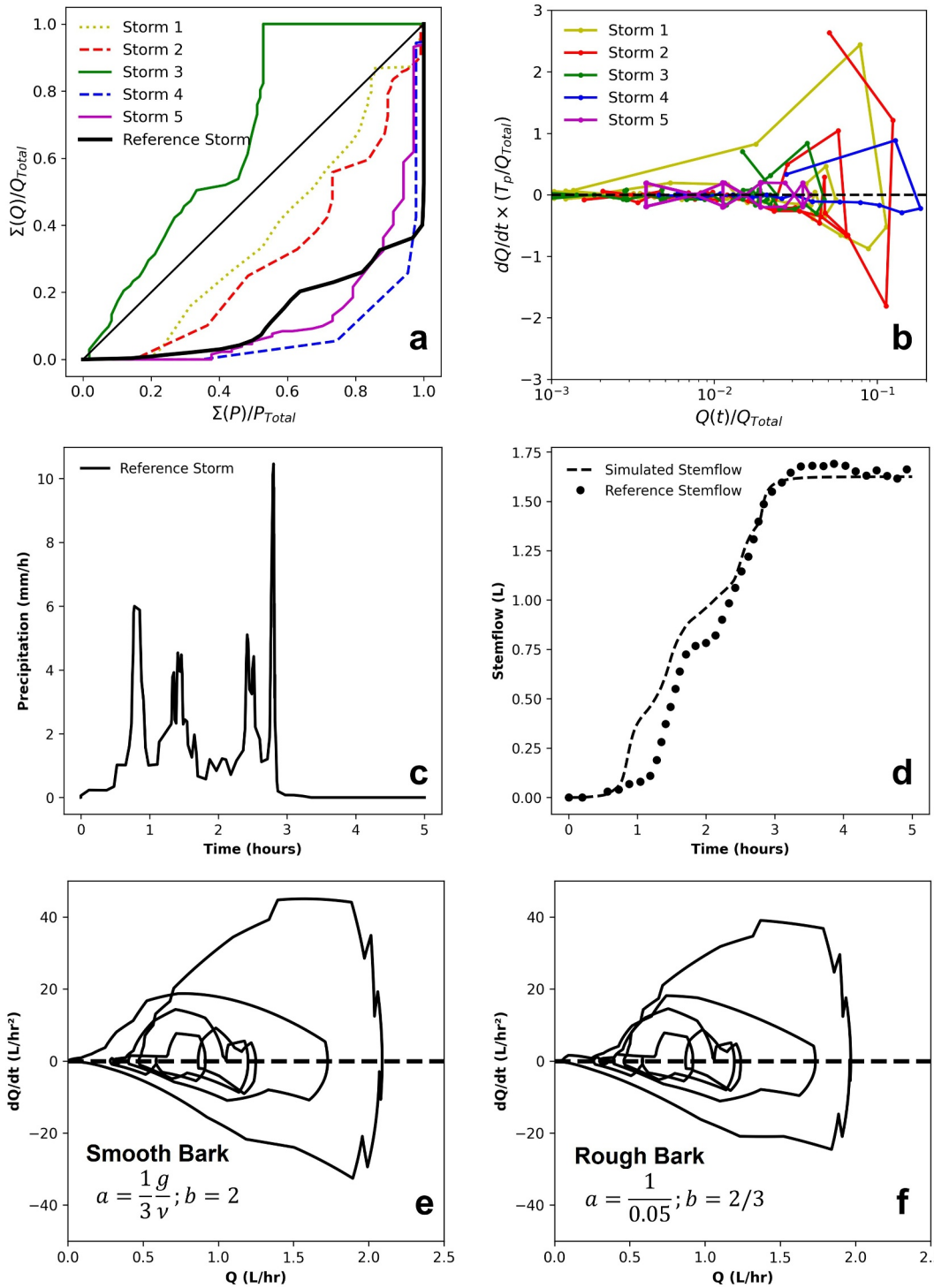

Figure 4. Panel (a): High resolution event-based precipitation $P(t)$ and stemflow $Q(t)$ digitized by us for five tropical storms (Germer et al., 2010) and for a single green ash tree in British Columbia (B. Turner et al., 2019). The data are presented as normalized cumulative precipitation (abscissa) against normalized cumulative stemflow (ordinate). The normalization of the abscissa and ordinates use total precipitation and total stemflow. The one-to-one line reflects perfect proportionality between stemflow and precipitation. Deviations from the one-to-one line are due to nonlinearities arising from stemflow hydrodynamics on short time scales. Panel (b): The phase space (i.e., dQ/dt vs. Q) of the normalized stemflow for the five tropical storms. Hysteresis, loops, and asymmetry in dQ/dt at a fixed Q are all due to stemflow hydrodynamics. Panel (c): The measured precipitation time series for the reference tree *Fraxinus pennsylvanica* Marshall (juvenile green ash). Panel (d): Comparison between the reservoir model (dashed) and the ultrasonic sensor measurements of cumulative stemflow (circles) assuming laminar and smooth bark. Panels (e)–(f): The modeled phase space is shown assuming smooth and laminar flow (e) and fully rough fully developed turbulent flow (f).

$$\frac{d(Vol)}{dt} = Q_{in} - S_w(\pi D_s H) - Q, \tag{28}$$

where $Vol = (\pi D_s H)h$ is the volume of surface water on the main stem, Q is the volume of flowing water per unit time at the base of the stem (i.e., the measured stemflow rate), and Q_{in} is the inflow rate of water onto the main stem generated from all the branches assumed to be linearly related to precipitation. The conservation of momentum is not explicitly solved in such spatially lumped models. However, the following considerations are made: (a) $Q = u_{avg}h(\pi D_s)$ (i.e., continuous sheet flow), (b) the solutions of the conservation of momentum equations under a set of idealized assumptions can be expressed as $u_{avg} = ah^b$, where a and b encode all the physics in the momentum balance. For a smooth laminar flow $u_{avg} = (1/3)(g/\nu)h^2$. For very large Re and $r/h \ll 1$, $f = 0.26(r/h)^{1/3}$ (i.e., Strickler scaling). It directly follows from definitions that

$$h = \left(\frac{Q}{a\pi D_s}\right)^{1/(b+1)}; Vol = \pi D_s H\left(\frac{Q}{a\pi D_s}\right)^{1/(b+1)}, \tag{29}$$

and that

$$\frac{dVol}{dt} = \frac{\pi^{b/(1+b)} D_s H}{1+b}(aD_s)^{-1/(1+b)} Q^{-b/(1+b)}\frac{dQ}{dt}. \tag{30}$$

Ignoring bark absorption momentarily (i.e. $S_w = 0$) and inserting these definitions into the conservation of water mass yields

$$B_2\frac{dQ}{dt} + Q = Q_{in}(t);\ B_2 = H\frac{(\pi D_s)^{b/(1+b)}}{1+b}\left(\frac{1}{a}\right)^{1/(1+b)}, \tag{31}$$

where B_2 is a characteristic transport time that depends on Re and bark roughness through coefficients a and b. Equation 31 describes how dQ/dt is related to Q (i.e., the phase-space) when excited by stochastic rainfall shocks producing $Q_{in}(t)$. The general solution of Equation 31 for any arbitrary inflow $Q_{in}(t)$ (constant or time dependent) is

$$Q(t) = \frac{1}{B_2}\exp\left(\frac{-t}{B_2}\right)\left[\int \exp\left(\frac{t}{B_2}\right) Q_{in}(t)dt + B_3\right], \tag{32}$$

where B_3 is an integration constant determined from the initial conditions. For a constant Q_{in} and assuming $Q(0) = 0$ (no stemflow before Q_{in}), the general solution can be expressed as

$$Q(t) = Q_{in}\left[1 - \exp\left(\frac{-t}{B_2}\right)\right]. \tag{33}$$

In this case, B_2 represents the e-folding time for water sourced from branches to be realized at the base of the tree. This theoretical result hints that $Q(t)/Q_{in}$ primarily depends on properties of stemflow hydrodynamics that control the e-folding time. It is this finding that inspired the use of a unit hydrograph (UH) approach to be described later on.

Figure 4 compares the stemflow model calculations with high frequency data for the aforementioned *Fraxinus pennsylvanica* Marshall (green ash) tree with $H = 7.8$ m and $D_s = 0.108$ m. The model calculations assume that $a = (1/3)(g/\nu)$, $b = 2$ (i.e., smooth laminar flow), and $S_p = 0$. While green ash does not have a smooth bark, the flow is approximated by a laminar state for hydrodynamically smooth conditions (i.e., the viscous sublayer exceeds the micro-roughness). To convert incident rainfall into Q_{in}, the following assumptions were made:

(i) using published allometric relations for green ash (Peper et al., 2014), the crown diameter W was estimated to be 2 m for the reported stem diameter $D_s = 0.1$ m;

(ii) some 10% of the crown area was then presumed to contribute to stemflow generation onto the main stem (i.e., a slender tree assumption in Figure 2). As a plausibility check, this computed water generating area turns out to be about 13% of the surface bark area of the main stem (i.e., $\pi D_c H$).

With these assumptions, $Q_{in}(t) = (0.13\pi D_c H)P(t)$, where measured $P(t)$ was used in the model calculations (also shown in Figure 4). Given the simplifying assumptions, the agreement between measured and modeled stemflow is acceptable.

The ultrasonic sensor is known not to be responsive to small variations in stemflow for low water levels (B. Turner et al., 2019). This lack of responsiveness means that the measured stemflow in the first hour or so after the commencement of rainfall may be underestimated. The relation between u_{avg} and h is likely to be more complex than a power-law with its own lags when the expanded conservation of momentum is considered. Moreover, such analysis suffers from equi-finality issues—meaning that different choices of a and b fit the measured high frequency cumulative stemflow reasonably. To underscore this point, the calculations were repeated with $b = 2/3$ (turbulent) and after optimizing for a (optimized value $a = 1/0.05$, very rough), the model can describe the cumulative stemflow time series reasonably (not shown) with comparable root-mean squared value to the laminar/smooth bark solution. Inspection of the corresponding phase-space (i.e. dQ/dt vs. Q) reveals some differences between the laminar/smooth bark and the turbulent rough/bark solutions featured in Figure 4 despite comparable statistical fit to the cumulative stemflow series. These differences include the extremes of dQ/dt (positive or negative) for high Q and the rapid initial increase in dQ/dt with increasing Q being larger for the smooth case when compared to the rough turbulent case. More interestingly here is that the computed phase space patterns by this model are qualitatively similar to those reported for the tropical forests. At large Q, positive dQ/dt exceeds its negative counterparts, and the hysteresis loops appear similar across the figures suggestive of similarity in stemflow hydrodynamics. Figure 5 presents other outcomes from the model calculations including h, u_{avg}, Re, and We. In all calculations, $h/H \ll 1$ and the thin film approximation holds when the path length is commensurate with H (as is assumed here). When setting $l = H$ (maximum possible longitudinal wavelength), the $We > 10$ so that surface tension effects may be ignored for most of the "active" stemflow generation period. It is interesting to compare the computed u_{avg} with other field experiments that have offered estimates of stemflow velocity (Zhang et al., 2023). The modeled u_{avg} here appears to be one order of magnitude smaller than the maximal stemflow velocities reported in a recent study (Zhang et al., 2023) on rough bark of pines. In this field study, maximal velocities from injected water onto the bark of burned and intact pine trees were reported in the fissures of the rough bark (i.e., the entire cross-sectional area $= \pi D_s$ was not accessible to stemflow). Hence, it is not surprising that the computed u_{avg} here is smaller than the maximal velocities reported from these fissures. The model calculations also show that the flow maintains its laminar state (i.e., Re $\leq$ 500) throughout this storm consistent with the assumed values of $b = 2$ and $a = g/(3\nu)$.

5. Open Problems and Future Research Directions

While the material reviewed here focused on depth-averaged models, there are numerous and daunting challenges that need to be confronted for a complete description of stemflow hydrodynamics. These challenges may be partly addressed by requiring dedicated experiments, theories, and numerical simulations to resolve them. A subset of those challenges are listed below setting a research agenda for the future and potentially inspiring dissertation topics.

5.1. Fluid Properties

The addition of surfactants due to plant residue (e.g., acids), dust particles (e.g., salt), or exuded sap (e.g., resin) can cause foam or soapy-like flow to occur as shown in Figure 1. This soapy behavior can disrupt the so-called Newtonian fluid approximation, which implies that σ and ν are no longer constant. The occurrences of such bubbling has been reported in other studies (Magyar et al., 2021). In fact, an album of pictures of foam generation across several trees during an intense rainfall can be seen in a blog by J. West (2010). The intense rainfall, the leaching of surfactants along with air entrainment due to local turbulence generation as water is rapidly routed along the stem surface can contribute to such foam-like behavior.

Currently, the rheological properties of stemflow relating the viscous stress and strain rate or velocity gradients under different flow conditions and surfactants has also not been explored and deserve a closer inspection.

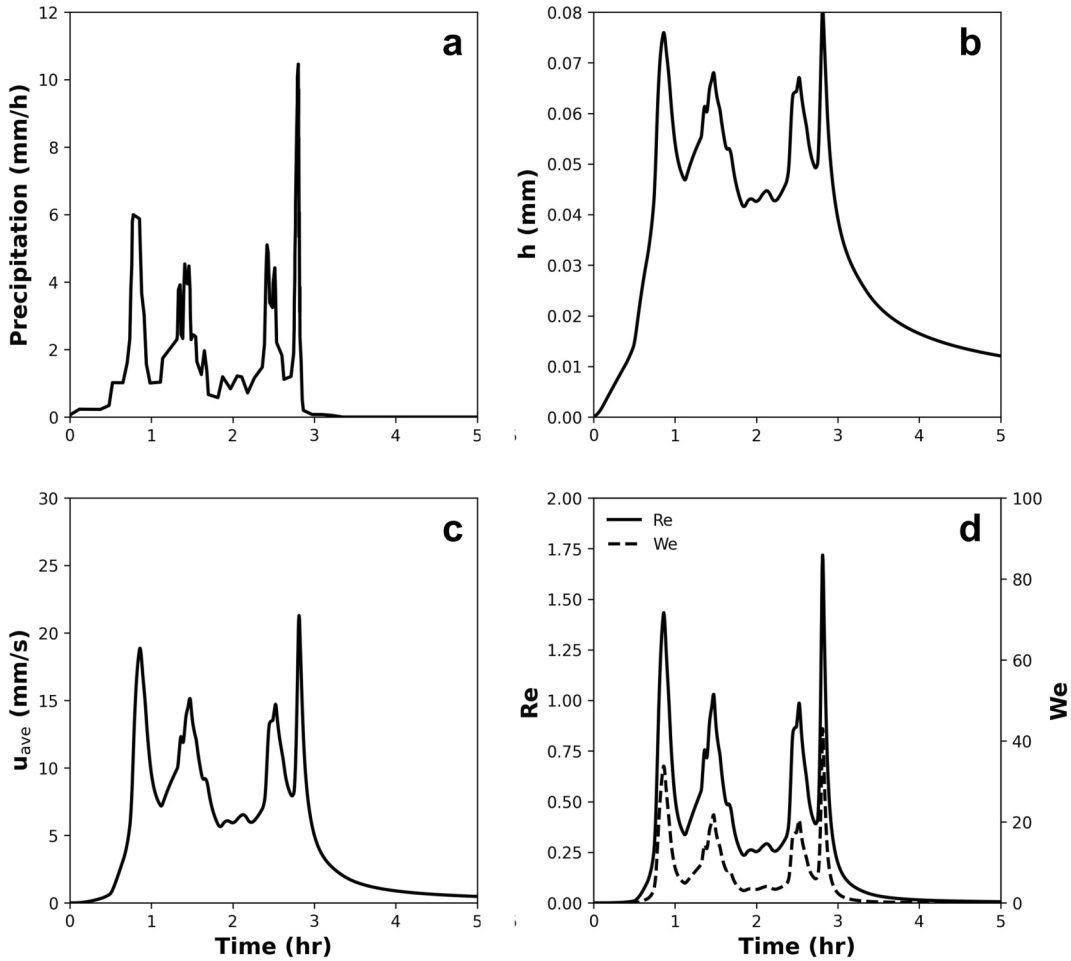

Figure 5. Top left: The measured $P(t)$ driving stemflow generation for a *Fraxinus pennsylvanica* Marshall (juvenile green ash) tree (B. Turner et al., 2019). Top right: Modeled h using the laminar approximation for smooth bark. For reference, the capillary length $l_{cap} = 2.8$ mm. Bottom left: The variation of modeled u_{avg} as a function of time. Bottom right: The computed Reynolds number Re derived from modeled u_{avg} and h and the Weber number We assuming $l = H$. Note the low Re signifies laminar flow and high We suggests that surface tension effects can be ignored.

Likewise, other fluid properties such as σ also require quantification in the presence of high surfactants as surfactants reduce σ and modify key dimensionless numbers (e.g., We and Bo) in the expanded momentum balance.

5.2. Bark Hydraulic and Chemical Properties

The analysis here is suggestive that a sorptive term arising in the conservation of water mass depends on the bark hydraulic conductivity, its water retention, the antecedent water content, and bark porosity. Undoubtedly, quantifying such bark hydraulic properties require dedicated laboratory experiments to characterize them. Inferring such hydraulic properties for soil samples have a long tradition in soil physics such as the use of centrifuges. How to build on these established soil physics methods for bark elements has its own challenges. Likewise, inferring those bark properties in-situ may be another daunting task that requires innovative experiments. One way forward is to note that the bark hydraulic properties (e.g., $K(\theta)$, $c(\theta)$, etc…), gas diffusion properties, electrical conductivity properties, and thermal properties are not entirely independent as they all depend on the same pore structure within the woody bark. Percolation theories have established theoretical links between hydraulic and thermal properties (Hunt, 2005) that can be exploited given that thermal properties may be more readily available or accessible in field studies (Nicolai, 1986).

While a network model of stemflow solute transport has been developed for rough-barked trees with furrows (Tucker et al., 2020), experimental work is needed to explore how the effects of biotic factors such as branch

inclination angle and projected branch area influence bark wetting processes and leachate quantities of a given solute. Such work may use branch angle leaching experiments as a starting point. For instance, it was found that branch inclination angles had a detectable and statistically significant effect on branch leaching during winter with branches inclined at 20° above the horizontal (as opposed to branches angled at 5° or 38°) having both the largest leachate concentrations and fluxes (Levia & Herwitz, 2002). This is due to the inter-relation among the orthogonally projected branch area, branchflow residence time, and branchflow volumes.

One way forward is to use large-scale rainfall simulator experiments (Iida et al., 2021) with an added chemical component to monitor solute leaching (or uptake) for a suite of solutes from small trees inside the rainfall simulator system. The twinning of bark soaking experiments with high-resolution scanning electron microscopy (SEM) of bark surfaces would likely provide unique data on the interplay between bark roughness profiles and wetting processes. These SEM images permit the quantification of sub-millimeter roughness of bark and foliar surfaces that then can be examined in relation to interception storage capacities (Campellone et al., 2020). Finally, the use of X-ray photo-electron spectroscopy to characterize the surface chemistry of bark surfaces could provide unparalleled insights into the influence of surface chemistry on leaching (or uptake) in judiciously designed experiments. To date, this is an under-utilized technique in stemflow studies.

5.3. Physics of Surface Tension

Given the potential role of surface tension in stemflow hydrodynamics, the Young-Laplace equation employed here remains a hydrostatic approximation to the force balance at the air-water interface. In the case of a rapidly moving fluids (e.g., rapidly advancing front in the initial phase of stemflow), the force balance encapsulated by the Young-Laplace equation should be augmented with inertia and viscous forces as well. This augmentation can generalize the Young-Laplace equation to yield the so-called Rayleigh-Plesset expression (Plesset, 1948). These augmentations, which lead to a second-order nonlinear differential equation for R_s in time (instead of an algebraic expression as in the Young-Laplace equation) were not pursued here but their significance in stemflow hydrodynamics require quantification beginning with dedicated laboratory experiments. In laboratory settings, it is possible to control rainfall amounts and their distribution as well as the branching and micro-roughness of the model trees as already described elsewhere (Dunkerley, 2014a, 2014b). The logical expansion of such experiments is to use different fluids to minimize surface tension effects and fluid viscosity (e.g., addition of alcohol) and be able to image the advancing water fronts with high fidelity to assess the role of surface tension on water movement for the same rainfall patterns.

5.4. Capillary and Surface Tension Effects

In the early stages of stemflow or slow rainfall events, the film thickness may be proportional to the height of fissure channel l. For small fissures $l \leq O(l_{cap})$ surface tension forces can play an important role in the stemflow hydrodynamics. To address the capillary effects in the momentum balance, the capillary pressure must be incorporated into the normal stress balance at the water-air interface using the Young-Laplace equation or a generalization of it such as the Rayleigh-Plesset formulation. Through normal stress boundary conditions, capillary effects are coupled to the existing balance between fluid inertia and the gradients of pressure and viscous stresses in the liquid film. This introduces curvature terms with intrinsic geometrical nonlinearities that are in many cases beyond the scope of existing analytical solutions. In the limit of thin films, simplifying approximations may be used to obtain a momentum equation that includes capillary effects (see Equation 25). Despite the nonlinear nature of such equations, Xue and Stone (2022) have shown that equally complex phenomenon such as gravitational draining of liquid films on narrow substrates exhibit self-similar behavior and can be modeled analytically with similarity transformations.

Expanding such ideas to thin film dynamics in stemflows can lead to the development of a new class of analytical or approximate solutions. In terms of experiments and specific laboratory measurements, it is possible to control rainfall amounts and their distribution as well as branching and micro-roughness along with different fluids to test the effects of surface tension and fluid viscosity on the advancing water fronts. Similarly, by introducing patterned grooves on model barks in these lab experiments with grooves commensurate to l_{cap}, the interplay between capillary effect and the geometry of bark fissures can be explored.

10.1029/2024RG000857

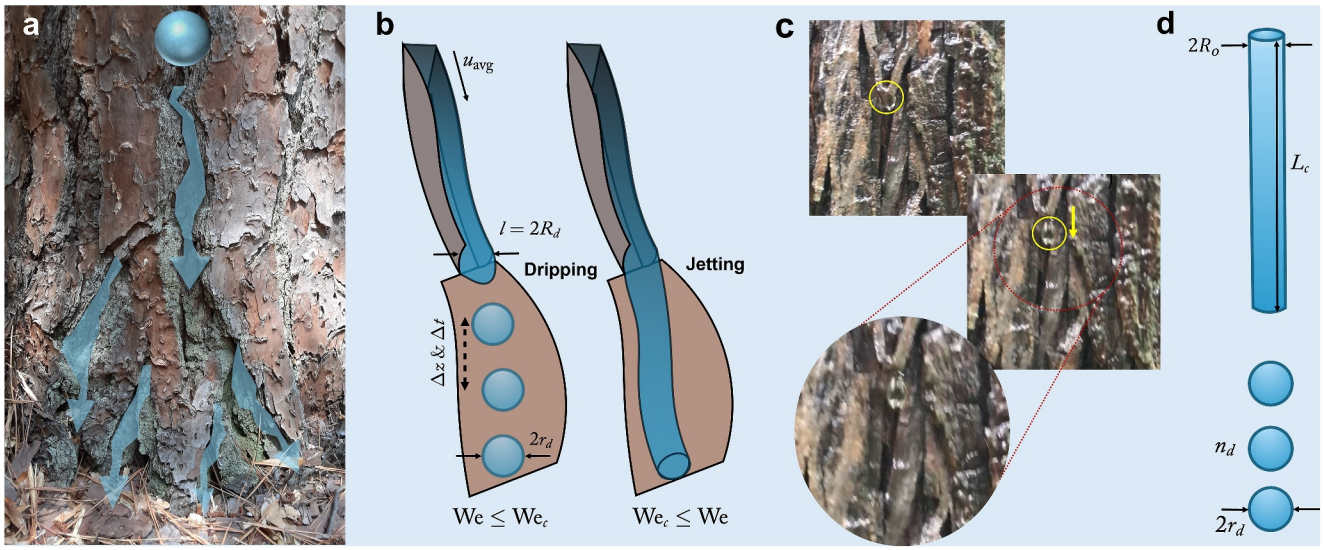

Figure 6. A liquid column that is trapped within a cylindrical bark fissure of a pine tree of effective diameter l can exit the fissure through either dripping or jetting. The cylindrical column may be initially held by capillary forces at the early stages of rainfall and stemflow generation, but once the gravitational forces exceed the capillary resistance, water will start dripping out of the fissure. The dripping mechanism observed in stemflow experiments such as the frames shown. Interested readers are referred to Movie S1 in Supporting Information that documents the dripping mechanism and the subsequent re-capture of the drop as stemflow on the rough, furrowed bark of a mockernut hickory tree (Video credit: D. Levia). Note that the drop size r_d exceeds the fissure radium $R_d = l/2$ in these frames. At later stages of the rainfall, the higher flux of stemflow generates enough momentum that leads to a transition from an intermittent dripping state to a continuous jetting flow. This dripping to jetting transition occurs above a certain critical Weber number.

5.5. Breakdown of the Sheet Flow

In the thin film approximation, the bark surface was assumed to be either smooth so that viscous forces dominate τ_W, or that $r/h \ll 1$ but the micro-roughness of the bark far exceeds the viscous sublayer thickness (i.e., fully rough flow). The viscous sublayer thickness scales with ν/u_*. These assumptions were necessary to illustrate some predictions from thin film theory as a first approximation. However, when r/h is no longer small, other considerations must be factored in. Those considerations can result in a break-down of the sheet flow approximation, of which dripping is the first noticeable mechanism. The pileup of water columns onto the stem and their release by dripping is a common occurrence in stemflow (see Supporting Information S1).

5.5.1. Dripping

The dripping phenomenon is a first indication that sheet flow approximations remain incomplete. The onset of the dripping phenomenon may be explained by a balance between gravitational and surface energies. As the height of accumulated water in a fissure space exceeds l_{cap}, the liquid starts dripping out of the fissure. As shown in Figure 6b, this intermittent ejection of liquid droplets can be quantified by temporal and spatial spacing between ejected droplets, Δt and Δz respectively. In the absence of viscous effects, droplets form at the exit of the fissure and detach through cyclic pinch off events with a period set by inertia-capillary timescale

$$\Delta t \sim \tau_{IC} \equiv \sqrt{\frac{\rho l^3}{\sigma}}. \tag{34}$$

Given an average travel velocity of u_{avg}, the detached droplets travel with a spacing of $\Delta z \sim u_{avg}\sqrt{\rho l^3/\sigma}$. To find the size of the detached droplets during the periodic dripping state, a connection to dripping nozzle experiments and early observations of Tate (1864) and Harkins and Brown (1919) can be drawn. A balance of the weight of the detached droplet and the supporting capillary force

$$\frac{4}{3}\pi r_d^3(\rho g) \simeq 2\pi R_d(\sigma) \tag{35}$$

indicates that $r_d/R_d \simeq (l_{\text{cap}}/2R_d)^{2/3}$. Such a scaling suggests that for fissures that are smaller than capillary length ($l = 2R_d < l_{\text{cap}}$) result in dripping droplets that can be significantly larger than the fissure radius R_d. Interestingly, stemflow observations support the finding that $r_d/R_d > 1$ as shown in the frames featured in Figure 6c and Movie S1. Such a dripping state continues until the rate of advection for fluid elements u_{avg}/R_d exceeds the rate of pinch-off events $1/\sqrt{\rho R_d^3/\sigma}$, which translates to a dripping-jetting transition when the Weber number $We \equiv \rho u_{\text{avg}}^2 R_d/\sigma$ exceeds a critical value We_c. Clanet and Lasheras (1999) have shown that for flow through cylindrical nozzles, such a critical Weber number depends on the Bond number based on the dimensions of the nozzle. While such a criterion can be extended to stemflow, one can also see the benefits of developing a similar criterion in a future study for dripping-jetting transition in tree-like fissures.

5.5.2. Jetting

In the jetting regime, there may be certain cases in which the ejected jet travels in the air and breaks up into individual droplets that then re-attach onto the stem. For an initial understanding of such capillary break-up, a cylindrical column of length L_c and radius R_o that breaks into n_d identical spherical droplets of size r_d is considered. The necessary condition is that R_o/r_d need to satisfy certain constraints for this spontaneous (i.e., with no energy input) breakup and those are briefly reviewed first.

Assuming no mass loss at the breakup, volume (or mass) conservation requires that the initial water in the volume of the cylinder of length L_c and radius R_o is conserved after drop formation. This volume conservation leads to

$$\pi R_o^2 L_c = n_d\left(\frac{4}{3}\pi r_d^3\right) \Rightarrow n_d = \frac{3}{4}\frac{L_c}{r_d}\frac{R_o^2}{r_d^2}. \tag{36}$$

The total surface area of the initial cylinder can now be compared to the total surface area of the drops. The surface area ratio is given by

$$\frac{2\pi R_o L_c}{n_d 4\pi r_d^2} = \frac{2}{3}\frac{r_d}{R_o}. \tag{37}$$

Spontaneous breakup requires that the final surface area of the spherical drops be smaller than the initial surface area of the cylinder. The energy or surface area minimization condition leads to $r_d > (3/2)R_o$. That is, the drop radius will be some 1.5 times larger than the initial cylindrical radius if the column breaks up into drops. To apply this finding to stemflow requires that water initially held in bark fissures be released with ample air space available for large radii to develop. Considerations using the Plateau-Rayleigh analysis is also suggestive that the cylindrical column travels some 6.6 R_o distance before pinching and breakup occurs. This is the necessary air volume that is required for droplets to experience free fall and re-attach along the stem.

5.6. Network Approaches

Early attempts approximate the topology of water flow as occurring within a network of connecting furrows embedded in the tree bark. The network is approximated by a directed graph that is characterized by edges that represent uninterrupted furrow and nodes. When a furrow is terminated, the water traveling down the furrow will cross the ridge and join the next furrow below it. The depth-averaged equations covered in this review can be formulated for a single furrow and then "upscaled" to the network level. The network topology connecting furrows serves as the spatial integrating kernel for the single furrow equations to arrive at water and solute fluxes out of the bark and into the soil. These approaches enable the role of network symmetry/asymmetry and its impacts on solute outflow from stems to be explored (Tucker et al., 2020). Key to this analysis is that conservation of water and solute mass along with some approximated conservation of momentum are written for a single furrow and the network topology drives the flow.

5.7. Spatial Patterns and Processes

Even within the continuum assumption, combining the expanded momentum balance with the water conservation equation results in a fourth-order partial differential equation that can be formulated in one- or two- dimensions.

In the one-dimensional case, it was experimentally shown that the inclusion of surface tension in the conservation of momentum leads to the formation of front instabilities characterized by a lateral wavelength λ_L given by Huppert (1982)

$$\lambda_L = \left(\frac{7.5A_o^{1/2}\sigma}{\rho g}\right)^{1/3}, \tag{38}$$

where A_o is the initial cross-sectional area of the water front featured in Figure 1. This lateral wavelength was shown to be independent of ν. The apparent "fingering" patterns on smooth bark may be interpreted from this force balance where irregularities along the bark surface or chance perturbations act to destabilize the equilibrium state as shown in Figure 1. The inclusion of viscous forces results in a partial differential equation that shares some similarity to a much more studied system—the so-called Kuramoto-Sivashinsky (KS) system (Yamada & Kuramoto, 1976). The KS system is given by

$$\frac{\partial u_{avg}}{\partial t} + u_{avg}\frac{\partial u_{avg}}{\partial x} + a_{KS}\frac{\partial^2 u_{avg}}{\partial x^2} + b_{KS}\frac{\partial^4 u_{avg}}{\partial x^4} = 0, \tag{39}$$

where a_{KS} and b_{KS} are coefficients related to viscosity and surface tension, respectively. In the original analysis of the KS system, both coefficients were set to unity. In this case, the KS system is known to exhibit spatio-temporal chaos that emerges through various bifurcations (Kalogirou et al., 2015). The KS system has also been shown to exhibit rich spatial pattern formation mechanisms in two-dimension (Kuramoto, 1984).

5.8. From Stemflow Time Series to Simplified Physics

With improvements in high resolution stemflow measurements, it may be possible to re-construct the correct nonlinearity associated with the phase-space of the dynamical system proposed here (Perona et al., 2000)—or the travel time statistics along the stem (e.g., UH). These two approaches have long tradition in hydrology.

5.8.1. Phase space reconstruction

A starting point to explore the phase space reconstruction method are laboratory experiments on artificial plants similar to those conducted by Dunkerley (2014a, 2014b). Such experiments are able to control the intensity and amount of rainfall as well as the antecedent initial moisture of the synthetic bark and thus offer a true test-case as to whether the complex stemflow hydrodynamics can be revealed from the phase-space of the data.

5.8.2. Unit hydrograph

Another line of inquiry proceeds to link the precipitation time series to stemflow time series using the concept of UH. In this case, the UH must be interpreted as a probability density function (PDF) of arrival times of water molecules to the stem base sourced from a single rainfall event having a uniform intensity over a fixed time period (e.g., 5 min). The UH must satisfy the normalization condition

$$\int_0^\infty UH(t)dt = 1. \tag{40}$$

The link between $P(t)$ and $Q(t)$ is then given by

$$Q(t) = \alpha_a \int_0^\infty P(s)\ UH(t-s)ds, \tag{41}$$

where α_a is a proportionality coefficient that depends on the total stemflow depth per total rainfall depth over the storm time scale. Based on the phase space analysis earlier discussed in Figure 4, it is clear that UH must be asymmetric to ensure the rise and fall of $Q(t)$ are not equal in magnitude for a uniform rainfall event. A number of PDF shapes may be offered that ensure this asymmetry—and a plausible choice explored here is a two parameter Gamma PDF given by

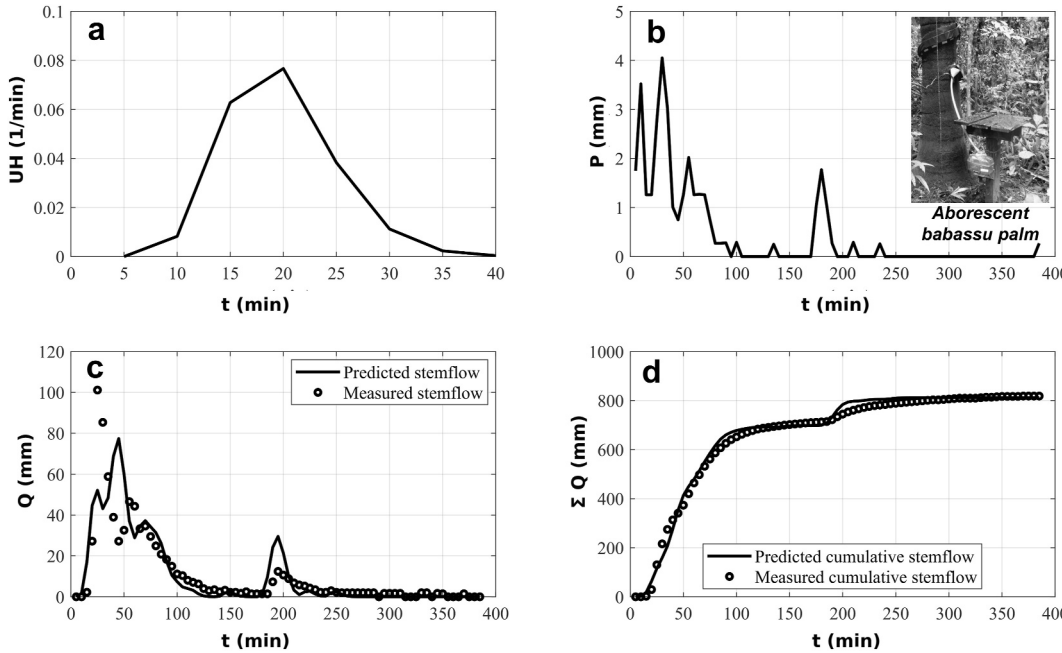

Figure 7. Panel (a) The Gamma probability density function unit hydrograph with shape parameter $k_g = 11.5$ and scale parameter $\theta_g = 1.5$. Panel (b) The measured time series of rainfall P reported in Germer et al. (2010) on 17 March 2005 (their original Figure 7). The inset photo is taken from Germer et al. (2010) for the babassu palm tree. Panel (c) Comparison between predicted and measured stemflow reported in Germer et al. (2010). Panel (d) The same as panel (c) but for cumulative stemflow.

$$UH(s) = \frac{1}{\Gamma(k_g)\,(\theta_g)^{k_g}}\, s^{k_g-1} \exp\left(-\frac{s}{\theta_g}\right), \tag{42}$$

where k_g and θ_g are the shape and scale parameters of the PDF.

To illustrate the utility of this approach, the five storms earlier discussed in Figure 5 were analyzed and good agreement between model calculations and measurements was found. The analysis for Storm 1, collected on 17 March 2005, is featured here as typical for such comparisons. In Figure 7, the computed shape parameter $k_g = 11.5$, scale parameter $\theta_g = 1.5$, and $\alpha_a = 122$ were determined from nonlinear optimization to minimize the root-mean squared error between modeled and measured cumulative stemflow. Given the acceptable agreement from this preliminary analysis, the UH concept may be used as a 'diagnostic' to contrast the effects of tree size, antecedent wetness conditions, differing bark roughness properties, and storm characteristics on parameters k_g, θ_g, and α_a. Clearly, these parameters may be related to a and b (and B_2) earlier discussed in the lumped model though theoretical links between the two approaches are better left for future studies.

5.9. Direct Measurement of Stemflow Depths

Developing methods to image h in space and time along the stem will enable the usage of the continuity equation to describe stemflow velocities, especially when the sorptive effects are small. The u_{avg} may be inverted from Equation 43 using

$$u_{avg} = -\frac{1}{h}\int_{x}^{x+\Delta x} \frac{\partial h}{\partial t} dx, \tag{43}$$

where x is the target position and Δx represents the image pixel size. Thus, relations between u_{avg} versus ah^b can then be used to assess the coefficients a and b and help delineate the nature of the flow (laminar or turbulent, smooth or rough).

6. Concluding Remarks

In plant hydraulics, stemflow hydrodynamics appears to be lagging when compared to other water delivery systems inside the plant such as the xylem or the phloem. No existing theory to date in stemflow rivals the predictive power of cohesion-tension (for the xylem) or osmoregulation (for the phloem) featured in Figure 1. Moreover, public data sets such as those of the TRY data base for plant traits (TRY DATA BASE A data base for global plant trait diversity, 2024), including vulnerability curves, exist for xylem flow but nothing commensurate to such a data base exist for stemflow. This deficiency may be partly explained by the absence of a general theory for stemflow hydrodynamics commensurate with the cohesion-tension theory and the associated vulnerability curves accompanying it. Tree geometry (i.e., H/W) does have some predictive power at long time scales and across wide ranging geometries as shown in Figure 2. However, at the storm time scale, the relation between rainfall and stemflow can be variable even for a preset tree geometry (or H/W) or in laboratory settings. Clearly, theories describing stemflow hydrodynamics applicable on short time scales are needed but are currently absent. This review sought to begin filling this knowledge gap by a bringing thin film theory into stemflow hydrodynamics. Thin film theory seeks to predict the time evolution of the thickness of a liquid film traversing on a solid surface based on the assumption that the length scales in the direction of motion are significantly larger than in the direction normal to the water surface. Thus, the application of thin-film theory to stemflow may be less controversial for impervious smooth bark or rough bark where water levels far exceed the micro-roughness values. It also sets the stage for flow within structured roughness elements when employing network theories as may occur in flow through inter-connected furrows where the characteristic length of the furrow far exceeds the water depth. However, these cases are only a subset of the general case where the sheet flow approximation breaks down, accumulation-ejection events can occur within bark fissures, and where surface tension can modify the force balance on a fluid element traversing along the stem. The review here covered few theoretical tactics when tackling these issues by drawing upon research successes in other fields. Thus, this review must be viewed as an embryonic first step, not a finality to how stemflow hydrodynamics should be represented.

The main message to be conveyed from this review is that stemflow hydrodynamics deserves its own rightful place as a new branch of fluid mechanics. Progress on stemflow hydrodynamics may well open up new vistas in engineering designs that utilize thin film theories, flow through disordered media, pattern formation and fluid instabilities, among others. It can become a fertile area for graduate student dissertations concerned with developing fundamentals, integrating vast knowledge from distinct disciplines, and innovating experiments (lab and field) or numerical simulations in a manner that maintains high societal impact, especially as the significance of stemflow is exponentially proliferating in the geosciences and other operational areas such as city planning and green infrastructure.

Data Availability Statement

In compliance with the FAIR Data guidelines, it is noted that this review is theoretical in nature and no new data were produced. All data sources are cited in the manuscript and repeated here for convenience.

- Data in Figure 2 were assembled from a global database (Sadeghi et al., 2020) along with published field experiments from isolated single-leader and multi-leader urban trees described in Schooling and Carlyle-Moses (2015) (the ordinate), Carlyle-Moses and Schooling (2015) (the abscissa), and laboratory measurements on wooden dowels from Dunkerley (2014a).
- Data in Figure 4 for the tropical ecosystem were published in the original Figure 7 by Germer et al. (2010). For the single green ash tree in British Columbia, data were published in the original Figures 6 and 8 by B. Turner et al. (2019).
- Data in Figure 7 are also published from the original Figure 7 by Germer et al. (2010).

Glossary

The Table below is a glossary of all the main symbols used along with their unit dimension. The $[M][L][T]$ convention is used where the three fundamental dimensions express dimensions of any physical quantity with $[M]$ indicating mass, $[L]$ indicating length, and $[T]$ indicating time.

Symbol	Description	Dimension
A_o	Initial cross-sectional area of a water front on an inclined slope	[L^2]
$A_s = \pi D_s H$	Surface area of the cylindrical stem	[L^2]
α_a	Proportionality coefficient that quantifies the ratio of total stemflow depth to total rainfall depth over the duration of a storm event, reflecting the efficiency of rainfall conversion into stemflow	[–]
α_d	Empirical coefficient that depends on flow geometry	[–]
B_2	Characteristic transport time in the lumped or nonlinear reservoir model	[T]
B_3	Integration constant determined from the initial conditions in the conservation of water mass	[–]
C, C_{sat}	Actual and saturation solute concentration for a leaching model	[M M^{-1}]
C_d	**Drag coefficient linking u_{avg}^2 to u_*^2**. It quantifies the resistance or drag experienced by an object moving through a fluid	[–]
$c(\theta)$	**Specific water capacity**: The ability of the bark to store water per unit change in water content, which is a function of the volumetric water content (θ) and describes how much water the bark can hold or release as the water content changes	[L^{-1}]
D_d	**Dispersive solute diffusion:** The process by which solute particles spread in a fluid, not due to random molecular motion (diffusion) but also because of the flow characteristics, such as velocity differences across the area orthogonal to the flow (mechanical dispersion)	[L^2/T]
D_m	**Molecular diffusion coefficient:** The rate at which molecules spread due to random motion (diffusion) within a medium	[L^2/T]
D_s	Diameter at the base	[L]
D_T	Total solute diffusion in water ($=D_m + D_d$)	[L^2/T]
$D(\theta)$	Liquid water diffusivity within the bark	[L^2/T]
η_p	**Porosity (p-norm of the η vector):** A measure of the void spaces (pores) in the bark relative to its total volume. It represents the capacity of the bark to hold water	[–]
F_g	Gravitational force	[M L/T^2]
f	Darcy-Weisbach friction factor proportional to C_d	[–]
g	Gravitational acceleration	[L/T^2]
g_f	A geometric factor that depends on the cross-sectional shape of the flow channel	[–]
h_N	**Nusselt depth**: This depth is associated with the flow (e.g., boundary layer thickness or depth of water), incorporating the effects of fluid viscosity, flow rate, and gravitational forces	[L]
$h(x, t)$	Depth of water at position x and time t	[L]
H	Tree height	[L]
k_c	Rate constant for solute leaching	[1/T]
k_g	**Shape parameter:** Influences the form or skewness of the probability density function (PDF)	[–]
$K(\theta)$	Unsaturated hydraulic conductivity of the bark	[L/T]
L	Transport distance	[L]
L_c	Length of cylindrical column in droplet breakup	[L]
l	**Longitudinal characteristic length scale:** Describes the wavelength of surface curvature affecting surface tension	[L]
l_{cap}	Capillary length	[L]
l_o	**Radial or vertical characteristic length scale:** Represents radial or vertical transport length in advection and diffusion	[L]
n_d	Number of identical spherical droplets of radius r_d	[–]
n_M	Manning's roughness coefficient	[T/$L^{1/3}$]
ν	**Kinematic viscosity:** describes the fluid's internal resistance to flow relative to its density. It is the ratio of dynamic viscosity (denoted as μ) to the fluid's density (ρ)	[L^2/T]
P, P_T	Precipitation and its accumulation for a given storm duration	[L]

Table
Continued

Symbol	Description	Dimension
P_{atm}	**Atmospheric pressure:** This is the pressure exerted by the Earth's atmosphere at sea level. In this context, $P_{atm} = 0$, meaning the equation is relative to the atmospheric pressure	[M/(L T^2)]
P_s	**Water pressure component:** It represents the pressure of the water at the curved air-water interface in the advancing stemflow front	[M/(L T^2)]
Q, Q_T	Actual and accumulated stemflow	[L^3]
q	**Water flux:** Volumetric flow rate per unit width	[L^2/T]
q_c	**Solute mass flux:** It describes how much solute is being transported down the tree trunk per unit area and time due to advection, diffusion, and dispersion	[M/L^2/T]
r	Mean protrusion height of bark roughness elements	[L]
r_d	Radius of identical spherical droplets	[L]
R_o	Radius of cylindrical column in droplet breakup	[L]
ρ	Water density	[M/L^3]
$\psi(\theta)$	**Unsaturated water potential:** It describes the energy required to extract water from the bark, which depends on the water content (θ). As the bark becomes wetter or drier (i.e., as θ changes), the unsaturated water potential (ψ) also changes	[L]
S_c	**Solute leaching flux:** The net rate at which solutes are added to stemflow as it moves down the tree	[M/(M T)]
S_I	**Intrinsic Sorptivity:** A measure of the bark's inherent ability to absorb water, independent of external factors like water content or initial moisture conditions	[L/T$^{1/2}$]
S_p	**Sorptivity of water onto the bark:** A measure of the bark's ability to absorb water	[L/T$^{1/2}$]
S_w	**Loss of water into the bark:** The rate of water movement driven by hydraulic conductivity and water potential gradients, indicating how water is absorbed or moves within the bark in the absence of a gravitational potential	[L/T]
σ	Surface tension of water = 0.072 N/m	[M/T^2]
τ_c	**Characteristic solute leaching time:** The time it takes to saturate water with solutes (e.g, potassium, calcium, magnesium)	[T]
τ_w	Wall shear stress (force per unit area exerted by a fluid on the bark surface)	[M/(L T^2)]
θ	Volumetric water content of the bark	[–]
θ_g	**Scale parameter:** Determines the spread or width of the probability density function (PDF)	[–]
θ_i	Water content before the arrival of the wetting front	[–]
θ_o	Water content at the bark surface after the arrival of the wetting front	[–]
u_{ave}	Depth-averaged velocity at x and t	[L/T]
u_*	**Friction velocity:** It is a measure of the velocity that corresponds to the kinematic shear stress $\left(\sqrt{\tau_w/\rho}\right)$ acting on the surface of the bark due to water flow	[L/T]
UH	**Unit Hydrograph:** Represents the probability of arrival times of water molecules at the base of a tree to a unit depth of rainfall over a specific duration. It is used to model stemflow dynamics at the base of the tree, measured over time	[1/T]
V_b	Total bark volume	[L^3]
V_m	Volume of water stored within the bark fissures	[L^3]
W	**Crown width:** The horizontal width of the tree's crown, typically measured as the maximum distance between the outer edges of the foliage. It provides an estimate of the tree's canopy size	[L]
x_o	$H/W - 0.8$	[L]
y_o	Ratio of stemflow at the base to incident rainfall	[%]
$1/R_s$	Twice the mean curvature of the water surface	[L^{-1}]

Acknowledgments
The authors thank two anonymous referees and A. Guswa for the numerous comments and suggested revisions. GK acknowledges support from the US National Science Foundation (NSF-AGS-2028633) and the US Department of Energy (DE-SC0022072).

References

Aboal, J., Morales, D., Hernández, M., & Jiménez, M. (1999). The measurement and modelling of the variation of stemflow in laurel forest in Tenerife, Canary Islands. *Journal of Hydrology*, *221*, 161–175. https://doi.org/10.1016/S0022-1694(99)00086-4

Anderson, M. L., Bassom, A. P., & Fowkes, N. (2006). Exact solutions of the Laplace–Young equation. *Proceedings of the Royal Society A: Mathematical, Physical and Engineering Sciences*, *462*(2076), 3645–3656. https://doi.org/10.1098/rspa.2006.1744

André, F., Jonard, M., & Ponette, Q. (2008). Influence of species and rain event characteristics on stemflow volume in a temperate mixed oak–beech stand. *Hydrological Processes: An International Journal*, *22*(22), 4455–4466. https://doi.org/10.1002/hyp.7048

Banavar, J., Maritan, A., & Rinaldo, A. (1999). Size and form in efficient transportation networks. *Nature*, *399*(6732), 130–132. https://doi.org/10.1038/20144

Beckett, H. A., Webb, D., Turner, M., Sheppard, A., & Ball, M. C. (2024). Bark water uptake through lenticels increases stem hydration and contributes to stem swelling. *Plant, Cell and Environment*, *47*(1), 72–90. https://doi.org/10.1111/pce.14733

Berman, A. D., Ducker, W. A., & Israelachvili, J. N. (1996). Origin and characterization of different stick-slip friction mechanisms. *Langmuir*, *12*(19), 4559–4563. https://doi.org/10.1021/la950896z

Bialkowski, R., & Buttle, J. (2015). Stemflow and throughfall contributions to soil water recharge under trees with differing branch architectures. *Hydrological Processes*, *29*(18), 4068–4082. https://doi.org/10.1002/hyp.10463

Bolster, D., Hershberger, R. E., & Donnelly, R. J. (2011). Dynamic similarity, the dimensionless science. *Physics Today*, *64*(9), 42–47. https://doi.org/10.1063/pt.3.1258

Bonetti, S., Manoli, G., Manes, C., Porporato, A., & Katul, G. (2017). Manning's formula and Strickler's scaling explained by a co-spectral budget model. *Journal of Fluid Mechanics*, *812*, 1189–1212. https://doi.org/10.1017/jfm.2016.863

Brown, G. (2002). The history of the Darcy-Weisbach equation for pipe flow resistance. *Environmental and Water Resources History*, *38*(7), 34–43. https://doi.org/10.1061/40650(2003)4

Brown, J., & Barker, A. (1970). An analysis of throughfall and stemflow in mixed oak stands. *Water Resources Research*, *6*(1), 316–323. https://doi.org/10.1029/WR006i001p00316

Buckingham, E. (1914). On physically similar systems; illustrations of the use of dimensional equations. *Physical Review*, *4*(4), 345–376. https://doi.org/10.1103/physrev.4.345

Câmara, L., & Neto, A. S. (2009). Network modeling of chromatography by stochastic phenomena of adsorption, diffusion and convection. *Applied Mathematical Modelling*, *33*(5), 2491–2501. https://doi.org/10.1016/j.apm.2008.07.013

Campellone, S. V., Levia, D. F., & Montalto, F. A. (2020). Differences in submillimetre surface morphology and canopy interception storage capacities of Gleditsia triacanthos L. (honeylocust) in relation to canopy phenophase and position. *Ecohydrology*, *13*(3), e2192. https://doi.org/10.1002/eco.2192

Cape, J., Brown, A., Robertson, S., Howson, G., & Paterson, I. (1991). Interspecies comparisons of throughfall and stemflow at three sites in northern Britain. *Forest Ecology and Management*, *46*(3–4), 165–177. https://doi.org/10.1016/0378-1127(91)90229-o

Carlyle-Moses, D., Iida, S., Germer, S., Llorens, P., Michalzik, B., Nanko, K., et al. (2018). Expressing stemflow commensurate with its eco-hydrological importance. *Advances in Water Resources*, *121*, 472–479. https://doi.org/10.1016/j.advwatres.2018.08.015

Carlyle-Moses, D., & Schooling, J. (2015). Tree traits and meteorological factors influencing the initiation and rate of stemflow from isolated deciduous trees. *Hydrological Processes*, *29*(18), 4083–4099. https://doi.org/10.1002/hyp.10519

Cayuela, C., Levia, D. F., Latron, J., & Llorens, P. (2019). Particulate matter fluxes in a Mediterranean mountain forest: Interspecific differences between throughfall and stemflow in oak and pine stands. *Journal of Geophysical Research: Atmospheres*, *124*(9), 5106–5116. https://doi.org/10.1029/2019JD030276

Cayuela, C., Llorens, P., Sánchez-Costa, E., Levia, D., & Latron, J. (2018). Effect of biotic and abiotic factors on inter and intra-event variability in stemflow rates in oak and pine stands in a Mediterranean mountain area. *Journal of Hydrology*, *560*, 396–406. https://doi.org/10.1016/j.jhydrol.2018.03.050

Chang, H.-C. (1994). Wave evolution on a falling film. *Annual Review of Fluid Mechanics*, *26*(1), 103–136. https://doi.org/10.1146/annurev.fluid.26.1.103

Cherry. (2024). BIM objects of Plants. Retrieved from https://www.bimobject.com/en/plants/product/cherry

Chikwendu, S. (1986). Calculation of longitudinal shear dispersivity using an N-zone model as $N \to \infty$. *Journal of Fluid Mechanics*, *167*, 19–30. https://doi.org/10.1017/s0022112086002707

Clanet, C., & Lasheras, J. C. (1999). Transition from dripping to jetting. *Journal of Fluid Mechanics*, *383*, 307–326. https://doi.org/10.1017/s0022112098004066

Crockford, R., & Richardson, D. (2000). Partitioning of rainfall into throughfall, stemflow and interception: Effect of forest type, ground cover and climate. *Hydrological Processes*, *14*(16–17), 2903–2920. https://doi.org/10.1002/1099-1085(200011/12)14:16/17<2903::aid-hyp126>3.0.co;2-6

D'Alessio, S., Pascal, J., & Jasmine, H. (2009). Instability in gravity-driven flow over uneven surfaces. *Physics of Fluids*, *21*(6), 062105. https://doi.org/10.1063/1.3155521

Darcy, H. (1856). *Les fontaines publiques de la ville de Dijon*. Dalmont.

de Saint-Venant, B. (1871). Theorie du mouvement non permanent des eaux, avec application aux crues des rivieres et a l'introduction de marees dans leurs lits. *Comptes Rendus des Seances de l'Academie des Sciences*, *36*, 148–154.

Dixon, H. H., & Joly, J. (1894). On the ascent of sap. *Proceedings of the Royal Society of London*, *57*, 3–5.

Dunkerley, D. (2014a). Stemflow on the woody parts of plants: Dependence on rainfall intensity and event profile from laboratory simulations. *Hydrological Processes*, *28*(22), 5469–5482. https://doi.org/10.1002/hyp.10050

Dunkerley, D. (2014b). Stemflow production and intrastorm rainfall intensity variation: An experimental analysis using laboratory rainfall simulation. *Earth Surface Processes and Landforms*, *39*(13), 1741–1752. https://doi.org/10.1002/esp.3555

Falkengren-Grerup, U., & Björk, L. (1991). Reversibility of stemflow-induced soil acidification in Swedish beech forest. *Environmental Pollution*, *74*(1), 31–37. https://doi.org/10.1016/0269-7491(91)90024-Q

Fischer, H. (1973). Longitudinal dispersion and turbulent mixing in open-channel flow. *Annual Review of Fluid Mechanics*, *5*(1), 59–78. https://doi.org/10.1146/annurev.fl.05.010173.000423

Ford, E., & Deans, J. (1978). The effects of canopy structure on stemflow, throughfall and interception loss in a young Sitka spruce plantation. *Journal of Applied Ecology*, *15*(3), 905–917. https://doi.org/10.2307/2402786

Fuenzalida, T. I., Bryant, C. J., Ovington, L. I., Yoon, H.-J., Oliveira, R. S., Sack, L., & Ball, M. C. (2019). Shoot surface water uptake enables leaf hydraulic recovery in avicennia marina. *New Phytologist*, *224*(4), 1504–1511. https://doi.org/10.1111/nph.16126

Galilei, G. (1914). *Dialogues concerning two new sciences*. Dover Publications Inc.

García-Ros, G., Alhama, I., & Morales, J. (2019). Numerical simulation of nonlinear consolidation problems by models based on the network method. *Applied Mathematical Modelling*, *69*, 604–620. https://doi.org/10.1016/j.apm.2019.01.003

Gauci, V., Pangala, S. R., Shenkin, A., Barba, J., Bastviken, D., Figueiredo, V., et al. (2024). Global atmospheric methane uptake by upland tree woody surfaces. *Nature*, *631*(8022), 796–800. https://doi.org/10.1038/s41586-024-07592-w

Germer, S. (2013). Development of near-surface perched water tables during natural and artificial stemflow generation by babassu palms. *Journal of Hydrology*, *507*, 262–272. https://doi.org/10.1016/j.jhydrol.2013.10.026

Germer, S., Werther, L., & Elsenbeer, H. (2010). Have we underestimated stemflow? Lessons from an open tropical rainforest. *Journal of Hydrology*, *395*(3–4), 169–179. https://doi.org/10.1016/j.jhydrol.2010.10.022

Gersper, P., & Holowaychuk, N. (1971). Some effects of stem flow from forest canopy trees on chemical properties of soils. *Ecology*, *52*(4), 691–702. https://doi.org/10.2307/1934160

Gonzalez-Ollauri, A., Stokes, A., & Mickovski, S. (2020). A novel framework to study the effect of tree architectural traits on stemflow yield and its consequences for soil-water dynamics. *Journal of Hydrology*, *582*, 124448. https://doi.org/10.1016/j.jhydrol.2019.124448

Gunther, B. (1975). Dimensional analysis and theory of biological similarity. *Physiological Reviews*, *55*(4), 659–699. https://doi.org/10.1152/physrev.1975.55.4.659

Haas, A., Pollak, T., & Aksel, N. (2011). Side wall effects in thin gravity-driven film flow—Steady and draining flow. *Physics of Fluids*, *23*. https://doi.org/10.1063/1.3604002.1063/1.3604002

Hanchi, A., & Rapp, M. (1997). Stemflow determination in forest stands. *Forest Ecology and Management*, *97*(3), 231–235. https://doi.org/10.1016/s0378-1127(97)00066-2

Harkins, W. D., & Brown, F. (1919). The determination of surface tension (free surface energy), and the weight of falling drops: The surface tension of water and benzene by the capillary height method. *Journal of the American Chemical Society*, *41*(4), 499–524. https://doi.org/10.1021/ja01461a003

Heaton, L., López, E., Maini, P., Fricker, M., & Jones, N. (2012). Advection, diffusion, and delivery over a network. *Physical Review E Statistical Nonlinear Soft Matter Physics*, *86*, 021905. https://doi.org/10.1103/PhysRevE.86.021905

Herwitz, S. (1987). Raindrop impact and water flow on the vegetative surfaces of trees and the effects on stemflow and throughfall generation. *Earth Surface Processes and Landforms*, *12*(4), 425–432. https://doi.org/10.1002/esp.3290120408

Hunt, A. G. (2005). Basic transport properties in natural porous media: Continuum percolation theory and fractal model. *Complexity*, *10*(3), 22–37. https://doi.org/10.1002/cplx.20067

Huppert, H. (1982). Flow and instability of a viscous current down a slope. *Nature*, *300*(5891), 427–429. https://doi.org/10.1038/300427a0

Iida, S., Wheeler, K. I., Nanko, K., Shinohara, Y., Sun, X., Sakai, N., & Levia, D. F. (2021). Canopy structure metrics governing stemflow funnelling differ between leafed and leafless states: Insights from a large-scale rainfall simulator. *Hydrological Processes*, *35*(8), e14294. https://doi.org/10.1002/hyp.14294

Ilek, A., Siegert, C. M., & Wade, A. (2021). Hygroscopic contributions to bark water storage and controls exerted by internal bark structure over water vapor absorption. *Trees*, *35*(3), 831–843. https://doi.org/10.1007/s00468-021-02084-0

Imamura, N., Levia, D., Toriyama, J., Kobayashi, M., & Nanko, K. (2017). Stemflow-induced spatial heterogeneity of radiocesium concentrations and stocks in the soil of a broadleaved deciduous forest. *Science of the Total Environment*, *599*, 1013–1021. https://doi.org/10.1016/j.scitotenv.2017.05.017

Jeffreys, H. (1930). The draining of a vertical plate. *Mathematical Proceedings of the Cambridge Philosophical Society*, *26*(2), 204–205. https://doi.org/10.1017/s0305004100015437

Jensen, K. H., Berg-Sørensen, K., Bruus, H., Holbrook, N. M., Liesche, J., Schulz, A., et al. (2016). Sap flow and sugar transport in plants. *Reviews of Modern Physics*, *88*(3), 035007. https://doi.org/10.1103/revmodphys.88.035007

Johnson, M., & Lehmann, J. (2006). Double-funneling of trees: Stemflow and root-induced preferential flow. *Écoscience*, *13*(3), 324–333. https://doi.org/10.2980/i1195-6860-13-3-324.1

Johnson, R. (1990). The interception, throughfall and stemflow in a forest in highland Scotland and the comparison with other upland forests in the UK. *Journal of Hydrology*, *118*(1–4), 281–287. https://doi.org/10.1016/0022-1694(90)90263-w

Kalogirou, A., Keaveny, E. E., & Papageorgiou, D. T. (2015). An in-depth numerical study of the two-dimensional Kuramoto–Sivashinsky equation. *Proceedings of the Royal Society A: Mathematical, Physical and Engineering Sciences*, *471*(2179), 20140932. https://doi.org/10.1098/rspa.2014.0932

Katul, G., Li, D., & Manes, C. (2019). A primer on turbulence in hydrology and hydraulics: The power of dimensional analysis. *Wiley Interdisciplinary Reviews: Water*, *6*(2), e1336. https://doi.org/10.1002/wat2.1336

Katul, G., Wiberg, P., Albertson, J., & Hornberger, G. (2002). A mixing layer theory for flow resistance in shallow streams. *Water Resources Research*, *38*(11), 32-1. https://doi.org/10.1029/2001wr000817

Katz, C., Oren, R., Schulze, E.-D., & Milburn, J. (1989). Uptake of water and solutes through twigs of *picea abies (l.)* Karst. *Trees*, *3*(1), 33–37. https://doi.org/10.1007/bf00202398

Klemm, O., Klemm, O., Kuhn, U., Beck, E., Katz, C., Oren, R., et al. (1989). Leaching and uptake of ions through above-ground Norway spruce tree parts. In *Forest decline and air pollution: A study of spruce (*picea abies*) on acid soils* (pp. 210–237). Springer.

Kodama, H. (1981). Automatic method for fabricating a three-dimensional plastic model with photo-hardening polymer. *Review of Scientific Instruments*, *52*(11), 1770–1773. https://doi.org/10.1063/1.1136492

Konrad, W., Katul, G., Roth-Nebelsick, A., & Jensen, K. H. (2019). Xylem functioning, dysfunction and repair: A physical perspective and implications for phloem transport. *Tree Physiology*, *39*(2), 243–261. https://doi.org/10.1093/treephys/tpy097

Kuramoto, Y. (1984). *Chemical oscillations, waves, and turbulence*. Dover Publications Inc.

Landy, J., Isleifson, D., Komarov, A., & Barber, D. (2014). Parameterization of centimeter-scale sea ice surface roughness using terrestrial LiDAR. *IEEE Transactions on Geoscience and Remote Sensing*, *53*(3), 1271–1286. https://doi.org/10.1109/tgrs.2014.2336833

Leff, J., Del Tredici, P., Friedman, W., & Fierer, N. (2015). Spatial structuring of bacterial communities within individual Ginkgo biloba trees. *Environmental Microbiology*, *17*(7), 2352–2361. https://doi.org/10.1111/1462-2920.12695

Levia, D. (2003). Winter stemflow leaching of nutrient-ions from deciduous canopy trees in relation to meteorological conditions. *Agricultural and Forest Meteorology*, *117*(1–2), 39–51. https://doi.org/10.1016/S0168-1923(03)00040-6

Levia, D., & Frost, E. (2003). A review and evaluation of stemflow literature in the hydrologic and biogeochemical cycles of forested and agricultural ecosystems. *Journal of Hydrology*, *274*(1–4), 1–29. https://doi.org/10.1016/S0022-1694(02)00399-2

Levia, D., & Germer, S. (2015). A review of stemflow generation dynamics and stemflow-environment interactions in forests and shrublands. *Reviews of Geophysics*, *53*(3), 637–714. https://doi.org/10.1002/2015RG000479

Levia, D., & Herwitz, S. (2000). Physical properties of water in relation to stemflow leachate dynamics: Implications for nutrient cycling. *Canadian Journal of Forest Research*, *30*(4), 662–666. https://doi.org/10.1139/x99-244

Levia, D., & Herwitz, S. (2002). Winter chemical leaching from deciduous tree branches as a function of branch inclination angle in central Massachusetts. *Hydrological Processes*, *16*(14), 2867–2879. https://doi.org/10.1002/hyp.1077

Levia, D., Keim, R., Carlyle-Moses, D., & Frost, E. (2011). Throughfall and stemflow in wooded ecosystems. In *Forest hydrology and biogeochemistry* (pp. 425–443). Springer.

Levia, D., Michalzik, B., Bischoff, S., Richter, S., & Legates, D. (2015). Differential stemflow yield from European beech saplings: The role of individual canopy structure metrics. *Hyrological Processes*, *29*, 43–51. https://doi.org/10.1002/hyp.10124

Levia, D., Van Stan, J., Mage, S., & Kelley-Hauske, P. (2010). Temporal variability of stemflow volume in a beech-yellow poplar forest in relation to tree species and size. *Journal of Hydrology*, *380*(1–2), 112–120. https://doi.org/10.1016/j.jhydrol.2009.10.028

Leyland cypress. (2024). Plants Leyland cypress. Retrieved from https://www.bimobject.com/en/plants/product/leylandcypress

Liang, W. (2020). Effects of stemflow on soil water dynamics in forest stands. In *Forest-water interactions* (pp. 349–370). Springer.

Llorens, P., Latron, J., Carlyle-Moses, D. E., Näthe, K., Chang, J. L., Nanko, K., et al. (2022). Stemflow infiltration areas into forest soils around American beech (*fagus grandifolia ehrh.*) trees. *Ecohydrology*, *15*(2), e2369. https://doi.org/10.1002/eco.2369

Loustau, D., Berbigier, P., Granier, A., & Moussa, F. E. H. (1992). Interception loss, throughfall and stemflow in a maritime pine stand. i. variability of throughfall and stemflow beneath the pine canopy. *Journal of Hydrology*, *138*(3–4), 449–467. https://doi.org/10.1016/0022-1694(92)90130-n

Magliano, P., Whitworth-Hulse, J., & Baldi, G. (2019). Interception, throughfall and stemflow partition in drylands: Global synthesis and meta-analysis. *Journal of Hydrology*, *568*, 638–645. https://doi.org/10.1016/j.jhydrol.2018.10.042

Magyar, D., Van Stan, J. T., & Sridhar, K. R. (2021). Hypothesis and theory: Fungal spores in stemflow and potential bark sources. *Frontiers in Forests and Global Change*, *4*, 623758. https://doi.org/10.3389/ffgc.2021.623758

Manfroi, O., Koichiro, K., Nobuaki, T., Masakazu, S., Nakagawa, M., Nakashizuka, T., & Chong, L. (2004). The stemflow of trees in a Bornean lowland tropical forest. *Hydrological Processes*, *18*(13), 2455–2474. https://doi.org/10.1002/hyp.1474

Martinez-Meza, E., & Whitford, W. (1996). Stemflow, throughfall and channelization of stemflow by roots in three Chihuahuan desert shrubs. *Journal of Arid Environments*, *32*(3), 271–287. https://doi.org/10.1006/jare.1996.0023

Matschonat, G., & Falkengren-Grerup, U. (2000). Recovery of soil pH, cation-exchange capacity and the saturation of exchange sites from stemflow-induced soil acidification in three Swedish beech (fagus sylvatica l.) forests. *Scandinavian Journal of Forest Research*, *15*(1), 39–48. https://doi.org/10.1080/02827580050160457

Moody, L. (1944). Friction factors for pipe flow. *Transactions of the American Society of Mechanical Engineers*, *66*(8), 671–684. https://doi.org/10.1115/1.4018140

Munch, E. (1930). *Die stoffbewegungen in der pflanze*. Gustav Fischer.

Murakami, S. (2024). Reduction in the ratio of stemflow to rainfall during heavy rain in two Japanese cedar stands and the influence on rainfall partitioning. *Journal of Hydrology*, *634*, 131100. https://doi.org/10.1016/j.jhydrol.2024.131100

Nanko, K., Keim, R. F., Hudson, S. A., & Levia, D. F. (2022). Throughfall drop sizes suggest canopy flowpaths vary by phenophase. *Journal of Hydrology*, *612*, 128144. https://doi.org/10.1016/j.jhydrol.2022.128144

Ni, D., & Leonard, J. (2005). A simplified kinematic wave model at a merge bottleneck. *Applied Mathematical Modelling*, *29*(11), 1054–1072. https://doi.org/10.1016/j.apm.2005.02.008

Nicolai, V. (1986). The bark of trees: Thermal properties, microclimate and fauna. *Oecologia*, *69*(1), 148–160. https://doi.org/10.1007/bf00399052

Nittmann, J., Daccord, G., & Stanley, H. (1985). Fractal growth viscous fingers: Quantitative characterization of a fluid instability phenomenon. *Nature*, *314*(6007), 141–144. https://doi.org/10.1038/314141a0

Olson, R., Reiners, W., Cronan, C., & Lang, G. (1981). The chemistry and flux of throughfall and stemflow in subalpine balsam fir forests. *Ecography*, *4*(4), 291–300. https://doi.org/10.1111/j.1600-0587.1981.tb01010.x

Parker, G. (1983). Throughfall and stemflow in the forest nutrient cycle. *Advances in Ecological Research*, *13*, 57–133. https://doi.org/10.1016/S0065-2504(08)60108-7

Parlange, J.-Y. (1975). On solving the flow equation in unsaturated soils by optimization: Horizontal infiltration. *Soil Science Society of America Journal*, *39*(3), 415–418. https://doi.org/10.2136/sssaj1975.03615995003900030019x

Peper, P. J., Alzate, C. P., McNeil, J. W., & Hashemi, J. (2014). Allometric equations for urban ash trees (Fraxinus spp.) in Oakville, Southern Ontario, Canada. *Urban Forestry and Urban Greening*, *13*(1), 175–183. https://doi.org/10.1016/j.ufug.2013.07.002

Perona, P., Porporato, A., & Ridolfi, L. (2000). On the trajectory method for the reconstruction of differential equations from time series. *Nonlinear Dynamics*, *23*, 13–33.

Pfautsch, S., Renard, J., Tjoelker, M. G., & Salih, A. (2015). Phloem as capacitor: Radial transfer of water into xylem of tree stems occurs via symplastic transport in ray parenchyma. *Plant Physiology*, *167*(3), 963–971. https://doi.org/10.1104/pp.114.254581

Philip, J. R. (1957). The theory of infiltration: 4. Sorptivity and algebraic infiltration equations. *Soil Science*, *84*(3), 257–264. https://doi.org/10.1097/00010694-195709000-00010

Pinos, J., Latron, J., Levia, D. F., & Llorens, P. (2021). Drivers of the circumferential variation of stemflow inputs on the boles of Pinus sylvestris l. (Scots pine). *Ecohydrology*, *14*(8), e2348. https://doi.org/10.1002/eco.2348

Plesset, M. (1948). Dynamics of cavitation bubbles. *Journal of Applied Mechanics*, *16*, 228–231.

Porporato, A. (2022). Hydrology without dimensions. *Hydrology and Earth System Sciences*, *26*(2), 355–374. https://doi.org/10.5194/hess-26-355-2022

Ptatscheck, P., Milne, P., & Traunspurger, W. (2018). Is stemflow a vector for the transport of small metazoans from tree surfaces down to soil? *BMC Ecology*, *18*(1), 43. https://doi.org/10.1186/s12898-018-0198-4

Puri, A., Kunadi, A., Pfefferle, D., Ghisalberti, M., & Thompson, S. (2024). Idealized branch sections and hydrodynamic analysis characterize rainfall partitioning. *Hydrological Processes*, *38*(6), e15194. https://doi.org/10.1002/hyp.15194

Rayleigh, L. (1915). The principle of similitude. *Nature*, *95*(2373), 202–203. https://doi.org/10.1038/095202c0

Reid, L., & Lewis, J. (2009). Rates, timing, and mechanisms of rainfall interception loss in a coastal redwood forest. *Journal of Hydrology*, *375*(3–4), 459–470. https://doi.org/10.1016/j.jhydrol.2009.06.048

Riegler, W. (1881). Beobachtungen über die abfuhr meteorischen wassers entlang den hochstämmen. *Mitteilungen aus dem Förstlichen Versuchswesen Österreichs*, *2*, 234–246.

Roth, B. E., Slatton, K. C., & Cohen, M. J. (2007). On the potential for high-resolution lidar to improve rainfall interception estimates in forest ecosystems. *Frontiers in Ecology and the Environment*, *5*(8), 421–428. https://doi.org/10.1890/060119

Roth-Nebelsick, A., Ebner, M., Miranda, T., Gottschalk, V., Voigt, D., Gorb, S., et al. (2012). Leaf surface structures enable the endemic namib desert grass stipagrostis sabulicola to irrigate itself with fog water. *Journal of the Royal Society interface*, *9*(73), 1965–1974. https://doi.org/10.1098/rsif.2011.0847

Sadeghi, S. M. M., Gordon, D. A., & Van Stan, J. T. (2020). A global synthesis of throughfall and stemflow hydrometeorology. In *Precipitation partitioning by vegetation: A global synthesis* (pp. 49–70). Springer.
Scholle, M., & Aksel, N. (2001). An exact solution of visco-capillary flow in an inclined channel. *Zeitschrift für angewandte Mathematik und Physik ZAMP*, *52*(5), 749–769. https://doi.org/10.1007/PL00001572
Scholle, M., & Aksel, N. (2003). Thin film limit and film rupture of the visco-capillary gravity-driven channel flow. *Zeitschrift für angewandte Mathematik und Physik ZAMP*, *54*(3), 517–531. https://doi.org/10.1007/s00033-003-2090-z
Schooling, J., & Carlyle-Moses, D. (2015). The influence of rainfall depth class and deciduous tree traits on stemflow production in an urban park. *Urban Ecosystems*, *18*(4), 1261–1284. https://doi.org/10.1007/s11252-015-0441-0
Schwärzel, K., Ebermann, S., & Schalling, N. (2012). Evidence of double-funneling effect of beech trees by visualization of flow pathways using dye tracer. *Journal of Hydrology*, *470*, 184–192.
Segel, L., & Edelstein-Keshet, L. (2013). A primer on mathematical models in biology. In *Chap. 2*. Society for Industrial and Applied Mathematics. https://doi.org/10.1137/1.9781611972504
Su, L., Qi, L., Zhuang, W., & Zhang, Y. (2023). Contrasting effects of low-severity fire on stemflow production between coexisting pine and oak trees. *Science of the Total Environment*, *858*, 159885. https://doi.org/10.1016/j.scitotenv.2022.159885
Sutera, S. P., & Skalak, R. (1993). The history of Poiseuille's law. *Annual Review of Fluid Mechanics*, *25*(1), 1–20.
Tate, T. (1864). On the magnitude of a drop of liquid formed under different circumstances. *The London, Edinburgh and Dublin Philosophical Magazine and Journal of Science*, *27*(181), 176–180. https://doi.org/10.1080/14786446408643645
Taylor, G. I. (1953). Dispersion of soluble matter in solvent flowing slowly through a tube. *Proceedings of the Royal Society of London. Series A. Mathematical and Physical Sciences*, *219*(1137), 186–203.
Taylor, G. I. (1954). The dispersion of matter in turbulent flow through a pipe. *Proceedings of the Royal Society of London. Series A. Mathematical and Physical Sciences*, *223*(1155), 446–468.
Thompson, D. (1915). Galileo and the principle of similitude. *Nature*, *95*(2381), 426–427. https://doi.org/10.1038/095426a0
Tischer, A., Michalzik, B., & Lotze, R. (2020). Nonuniform but highly preferential stemflow routing along bark surfaces and actual smaller infiltration areas than previously assumed: A case study on european beech (fagus sylvatica l.) and sycamore maple (acer pseudoplatanus l.). *Ecohydrology*, *13*(6), e2230. https://doi.org/10.1002/eco.2230
TRY DATA BASE. (2024). TRY DATA BASE a data base for global plant trait diversity. Retrieved from https://www.try-db.org/TryWeb/Home.php
Tucker, A., Levia, D., Katul, G., Nanko, K., & Rossi, L. (2020). A network model for stemflow solute transport. *Applied Mathematical Modelling*, *88*, 266–282. https://doi.org/10.1016/j.apm.2020.06.047
Turner, B., Hill, D., Carlyle-Moses, D., & Rahman, M. (2019). Low-cost, high-resolution stemflow sensing. *Journal of Hydrology*, *570*, 62–68. https://doi.org/10.1016/j.jhydrol.2018.12.072
Turner, R., Panciera, R., Tanase, M., Lowell, K., Hacker, J., & Walker, J. (2014). Estimation of soil surface roughness of agricultural soils using airborne LiDAR. *Remote Sensing of Environment*, *140*, 107–117. https://doi.org/10.1016/j.rse.2013.08.030
Van Bel, A. (1990). Xylem-phloem exchange via the rays: The undervalued route of transport. *Journal of Experimental Botany*, *41*(6), 631–644. https://doi.org/10.1093/jxb/41.6.631
Van Stan, J., Dymond, S., & Klamerus-Iwan, A. (2021). Bark-water interactions across ecosystem states and fluxes. *Frontiers in Forests and Global Change*, *4*, 660662. https://doi.org/10.3389/ffgc.2021.660662
Van Stan, J., Van Stan, J.-H., & Levia, D. (2014). Meteorological influences on stemflow generation across diameter size classes of two morphologically distinct deciduous species. *International Journal of Biometeorology*, *58*(10), 2059–2069. https://doi.org/10.1007/s00484-014-0807-7
Voigt, G. (1960). Distribution of rainfall under forest stands. *Forest Science*, *6*(1), 2–10.
Voigt, G., & Zwolinski, M. (1964). Absorption of stemflow by bark of young red and white pines. *Forest Science*, *10*(3), 277–282.
Washington Post. (2024). Picture of foamy bubbles form on the bark of a tree along Sligo Creek in Silver Spring. Retrieved from https://www.washingtonpost.com/dc-md-va/2023/02/20/tree-spit-and-bug-spit
West, G. (2018). *Scale: The universal laws of life, growth, and death in organisms, cities, and companies*. Penguin.
West, J. (2010). Nature notes: Tree foam. Retrieved from http://ramblinghemlock.blogspot.com/2010/09/first-website.html
Whittaker, R., & Woodwell, G. (1967). Surface area relations of woody plants and forest communities. *American Journal of Botany*, *54*(8), 931–939. https://doi.org/10.1002/j.1537-2197.1967.tb10717.x
Wu, M.-D., Jiang, Z.-Y., Yang, X., Yeerbolati, B., Huang, L., Zhong, Y.-Y., et al. (2024). Global quantitative synthesis on the patterns and drivers of funneling ratio and enrichment ratio for stemflow. *Catena*, *244*, 108253. https://doi.org/10.1016/j.catena.2024.108253
Xue, N., & Stone, H. A. (2022). Gravitational drainage on a vertical substrate of a narrow width. *Physical Review Fluids*, *7*(1), 014001. https://doi.org/10.1103/physrevfluids.7.014001
Yamada, T., & Kuramoto, Y. (1976). A reduced model showing chemical turbulence. *Progress of Theoretical Physics*, *56*(2), 681–683. https://doi.org/10.1143/PTP.56.681
Yan, C., Chen, H.-Y., Lai, P.-Y., & Tong, P. (2023). Statistical laws of stick-slip friction at mesoscale. *Nature Communications*, *14*(1), 6221. https://doi.org/10.1038/s41467-023-41850-1
Zhang, Y., Wang, L., Yang, J., & Wang, Q. (2023). Quantification of the change in stemflow velocity and evaluation of its potential washing effects in a pine forest as affected by the wildfire in southwest China. *Plant and Soil*, *483*(1), 411–426. https://doi.org/10.1007/s11104-022-05752-3
Zhang, Y., Yao, W., Yuan, C., Chen, N., & Levia, D. F. (2024). Alterations of throughfall and stemflow chemistry by vegetation in China: Insights from a machine learning based meta-analysis. *Journal of Hydrology*, *641*, 131786. https://doi.org/10.1016/j.jhydrol.2024.131786